RSC Advances

REVIEW

View Article Online
View Journal | View Issue

Check for updates

Cite this: *RSC Adv.*, 2022, **12**, 35556

MnO_2-based materials for supercapacitor electrodes: challenges, strategies and prospects

Juyin Liu, Jiali Bao, Xin Zhang, Yanfang Gao,* Yao Zhang, Ling Liu*
and Zhenzhu Cao

Received 21st October 2022
Accepted 28th November 2022

DOI: 10.1039/d2ra06664e

rsc.li/rsc-advances

Manganese dioxide (MnO_2) has always been the ideal electrode material for supercapacitors due to its non-toxic nature and high theoretical capacity (1370 F g^{-1}). Over the past few years, significant progress has been made in the development of high performance MnO_2-based electrode materials. This review summarizes recent research progress in experimental, simulation and theoretical studies for the modification of MnO_2-based electrode materials from different perspectives of morphology engineering, defect engineering and heterojunction engineering. Several main approaches to achieve enhanced electrochemical performance are summarized, respectively increasing the effective active site, intrinsic conductivity and structural stability. On this basis, the future problems and research directions of electrode materials are further envisaged, which provide theoretical guidance for the adequate design and synthesis of MnO_2-based electrode materials for use in supercapacitors.

1. Introduction

In recent years, the rapid development of the global economy and the expanding industrialization of science and technology have led to the depletion of fossil energy sources and the production of large amounts of carbon dioxide emissions, which have a serious impact on the environment and human beings. In order to meet the demand for efficient energy storage systems, there is an urgent need to research and develop new electrochemical energy storage devices (EESDs) for energy conversion, which are suitable for different energy storage systems in multiple fields.[1] Supercapacitors (SCs), also known as electrochemical capacitors (ECs), have attracted wide attention as they are alternative to both conventional capacitors and secondary batteries with such features as high-power density, long cyclic stability, good rate capability and fast charge/discharge.[2,3] SCs have unique advantages so that make them show good perspectives for future applications in new energy technologies, such as smart and wearable electrical products, wind pitch devices and grid access systems for power grids, *etc.*[4–7] In addition, SCs can fill the gap between batteries and conventional capacitors.[1] They meet the demand for short-term acceleration in electric and hybrid vehicles by providing higher power density. The power density and energy density are represented by Ragone plot (Fig. 1).

Based on the energy storage mechanisms, SCs are generally defined in three major categories: electric double-layer capacitors (EDLCs), Faraday pseudo-capacitors and hybrid capacitors which are made from a combination of the above two. In EDLCs, carbon-based materials are common electrode materials, which through the adsorption and desorption of ions

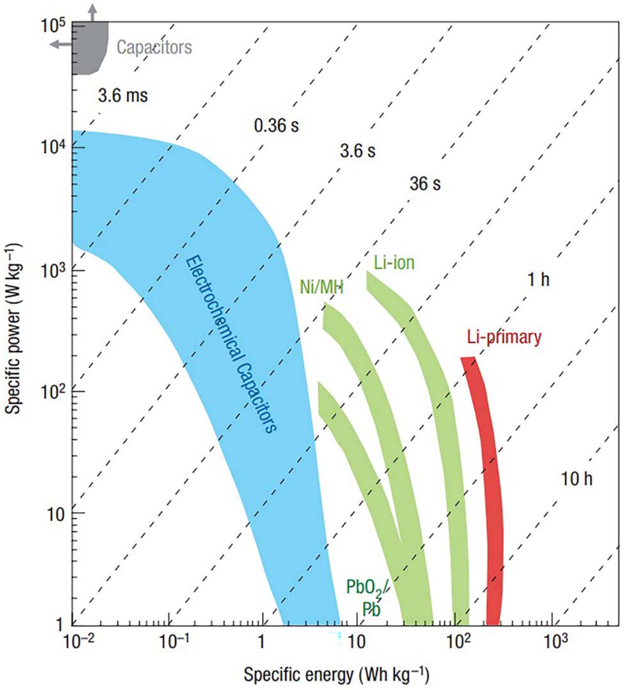

Fig. 1 Ragone plot of different electrochemical energy conversion systems. Reproduced with permission from ref. 1. Copyright 2008, Springer Nature.

School of Chemical Engineering, Inner Mongolia University of Technology, No. 49 Aimin Street, Xincheng District, Hohhot 010051, PR China. E-mail: yf_gao@imut.edu.cn; ll@imut.edu.cn

on the surface of the electrodes, complete the energy storage. Currently, many researchers have extensively studied carbon-based materials. Based on the traditional porous carbon materials, many new porous carbon materials have been prepared, which are able to achieve an increase in specific capacitance through the adjustment of the pore structure.[8,9] However, due to the limited physical space on the surface, its obtained energy density is lower.[10,11] In addition, the fast and reversible redox reacted inside the surface of electrodes in Faraday pseudo-capacitor that contribute to provide higher capacitance and increase energy density without impacting power density.[12] Nevertheless, the research on the matching degree of parameters between two electrodes (positive and negative) are not mature. Hence, it requires the development of good positive and negative electrode materials with high performance and compatibility.[13] In comparison, hybrid capacitors can achieve higher capacity and energy storage capability by combining two energy storage mechanisms of EDLCs and Faraday pseudo-capacitors.[14]

In general, the electrode materials of SCs are divided into EDLCs materials and pseudo-capacitor materials. Compared with the EDLCs materials, because of the high specific capacitance of the pseudo-capacitor materials, it plays an important role in the process of obtaining good capacitance and energy density. So far, many electrode materials based on transition metal oxides have been explored, such as TiO_2,[15] RuO_2,[16,17] V_2O_5,[18] Co_3O_4,[19] Fe_3O_4,[20] MoO_3 (ref. 21 and 22) and MnO_2.[23–26] Besides, spinel-based mixed transition metal oxides have also been investigated. Compared to the low electrical conductivity of oxides, spinel-based cobaltite has a variety of oxidation states and a higher electrical conductivity, which allows it to store more charge and thus achieve higher capacitive properties. These include $FeCo_2O_4$,[27–29] $ZnCo_2O_4$,[30–32] $CuCo_2O_4$,[33–35] $MnCo_2O_4$,[36–38] *etc.* MnO_2 has received great attention, because of its low price, low toxicity, high theoretical capacity (1370 F g^{-1}) and good environmental compatibility, *etc.*[39] But the electronic conductivity and structural stability of MnO_2 is poor, and there are some shortcomings such as the manganese (Mn) element is easily dissolved in the electrolyte, which limits the development and application of MnO_2-based electrode materials.[40] Therefore, researchers have usually worked on combining MnO_2 with highly conductive substrates (*e.g.*, metals or carbon-based materials) in order to enhance the whole performances. A series of MnO_2-based composites have been designed, including MnO_2/precious metal (gold, silver) composites,[41–43] MnO_2/transition metal (Cu, Ni, Mn) composites,[44–47] MnO_2/graphene composites,[48–50] MnO_2/carbon nanotube (CNT) composites,[51,52] MnO_2/porous carbon composites,[53,54] *etc.* Up to now, MnO_2-based materials have got good experiment and calculation results in aspects of enhanced electrical conductivity and improved specific surface area, and they have also been reviewed extensively from different perspectives. Our primary intention is to summarize the various engineering strategies in MnO_2-based electrode materials through reference and guidance for the unique design and preparation of MnO_2-based electrodes by specifically.

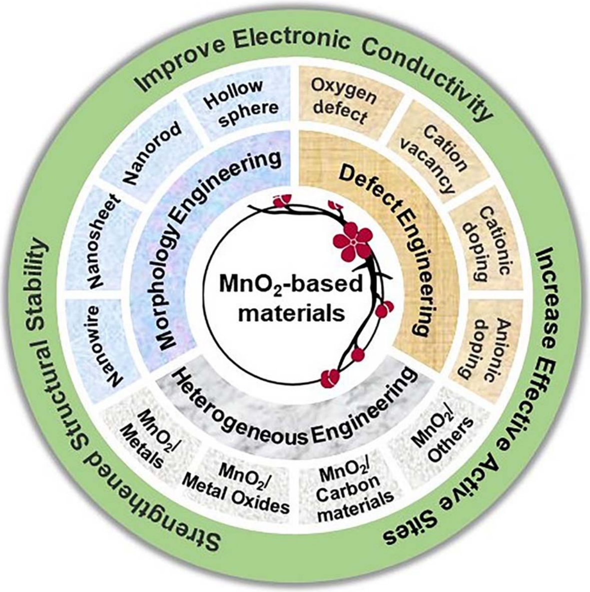

Fig. 2 Different engineering strategies to improve electrochemical performance.

In this review, we intend to conduct an in-depth investigation and comprehensive overview of the crystal structures and energy storage mechanisms of MnO_2-based electrode materials firstly. In addition, the problems which limit the application of MnO_2-based electrode materials are proposed, and several examples are combined to summarize and compare different engineering strategies that can improve the performance of MnO_2-based SCs (Fig. 2). Through in-depth research on improving the electrical conductivity and structural stability of MnO_2, and providing effective active sites for electrolyte cations. Finally, we give the overall summary of MnO_2-based electrode materials as well as the future outlook.

2. Types of MnO_2 crystal structures

In general, MnO_2 consists of $[MnO_6]$ octahedral unit, which is composed of one Mn atom and six oxygen (O) atoms. These $[MnO_6]$ octahedral units are connected to each other in different ways through shared angles and shared chains and so it shows a variety of tunnel and chain structures, which correspond to different crystal structures.[55] Among them, the crystal form of MnO_2 are mainly included: α-MnO_2, β-MnO_2, δ-MnO_2, γ-MnO_2, ε-MnO_2 and λ-MnO_2. The different crystal structures are shown in Fig. 3. According to the space structures, MnO_2 can be divided into three categories: one-dimensional (1D) tunnel structures, two-dimensional (2D) layered structures and three-dimensional (3D) network structures.[56]

The different MnO_2 have different structures and space groups, as shown in Table 1. α-MnO_2, β-MnO_2, γ-MnO_2 belong to the 1D tunnel structures where the lattice is all made up of shared chains and shared angles.[57,58] α-MnO_2 is a tetragonal crystal system, which belongs to the typical hollandite. It is crosslinked by the $[MnO_6]$ octahedron shared edge double

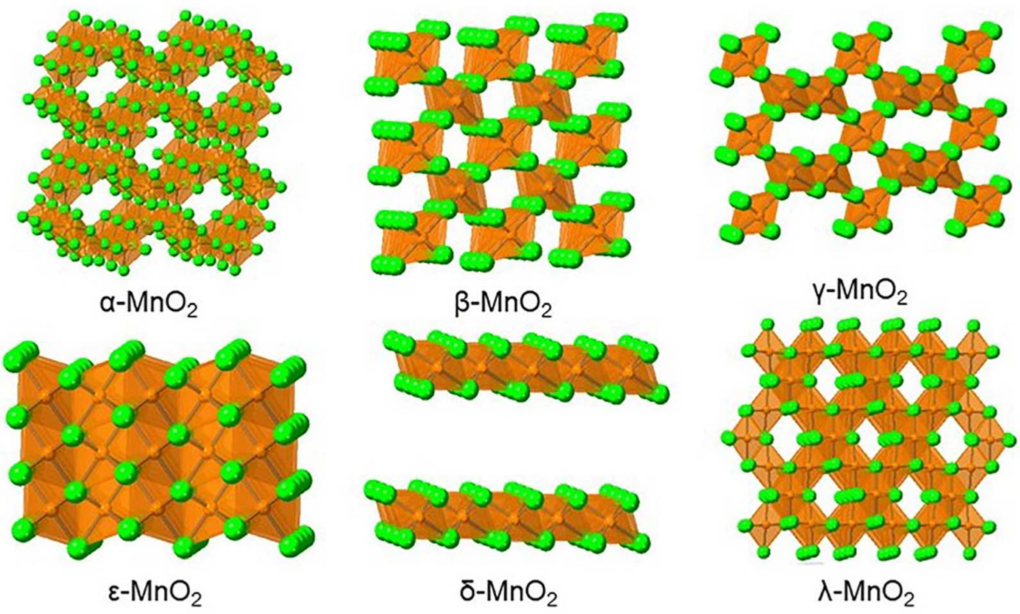

Fig. 3 Schematic diagram of the crystal structure of α-, β-, γ-, ε-, δ- and λ-MnO$_2$.

chain and forms 1D (2 × 2) tunnel structure through corner connections. The tunnel size of α-MnO$_2$ is 4.6 Å where most of the cations (*e.g.* K$^+$, Li$^+$, Na$^+$, Mg^{2+}, Ca^{2+}, *etc.*) can be allowed to pass through for its larger tunnel. β-MnO$_2$ is also a tetragonal crystal system with a rutile structure. The Mn atom is used as the centre of the [MnO$_6$] octahedron, and O atoms occupy its hexagon to arrange into a single-chain angular close-packed structure. The 1D (1 × 1) tunnel structure is formed by means of shared edge connections where each chain is connected by four similar chains. The narrow tunnel of β-MnO$_2$ is about 1.89 Å. It can only accommodate smaller ions, which is not conducive to the diffusion of ions. γ-MnO$_2$ is a hexagonal crystal system with a hexagonal close-packed structure.[59] γ-MnO$_2$ is the result of irregular alternating symbiosis of pyrolusite (1 × 1 type) and rhodochrosite (1 × 2 type). ε-MnO$_2$ has a structure that is comparable to γ-MnO$_2$, and it belongs to the hexagonal crystal system as well. The former is only connected by shared planes, which leads to a disordered appearance of its lattice and the formation of an irregular tunnel structure. Mn^{4+} is distributed in more than half of the [MnO$_6$] octahedral gap.[60] Both δ-MnO$_2$ and λ-MnO$_2$ are formed by using only the shared edges of [MnO$_6$] octahedron. δ-MnO$_2$ belongs to the monoclinic crystal system, which has 2D layered structure formed by the common edges of the [MnO$_6$] octahedron. It has a large interlayer distance of about 7 Å, which can allow a large number of water molecules, metal cations and other substances to pass through. Consequently, δ-MnO$_2$ is beneficial to the migration of ions/substances. λ-MnO$_2$ is a spinel structure, which is similar to γ-MnO$_2$. After the irregular alternating growth of pyrolusite and rhodochrosite, it forms a 3D (1 × 1 type) network structure, which promotes charge transfer.

3. Energy storage mechanism of MnO$_2$

Electrochemical behaviors of MnO$_2$-based electrode materials are divided into two types according to their energy storage mechanisms: EDLCs materials and Faraday pseudo-capacitance materials. The properties are determined by the cations in the electrolyte which lead to different energy storage mechanisms of MnO$_2$-based electrode materials. For example, it usually shows pseudo-capacitive behavior in electrochemical

Table 1 Multiple parameters of MnO$_2$ crystal structures

Crystalline forms	Structure types	Space groups	Tunnels ($n \times m$)	Size (Å)	Ref.
α-MnO$_2$	Hollandite	*I*4/*m*	(2 × 2)	4.6	61
β-MnO$_2$	Pyrolusite	*P*4$_2$/*mnm*	(1 × 1)	1.89	62
γ-MnO$_2$	Distorted boehmite	—	(1 × 1)/(1 × 2)	1.89/2.3	63
δ-MnO$_2$	Birnessite	*C*2/*m*	(1 × ∞)	7.0	64
ε-MnO$_2$	—	*P*6$_3$/*mmc*	(1 × 1)/(1 × 2)	3D	65
λ-MnO$_2$	Spinel	*Fd*3*m*	(1 × 1) interconnected 3D networks	3D	66

performance tests when the charge–discharge process occurs in alkaline electrolytes or neutral electrolytes containing alkali metal ions (Li^+, Na^+, K^+, *etc.*).[67,68]

In the energy storage mechanism of EDLCs, MnO_2-based electrodes exhibit adsorption/desorption activities over the material surface. After immersing the electrode in electrolyte, a tight charge layer is formed around the electrode surface by applying a certain voltage between the positive and negative electrodes, which promotes the separation of charges.[69–71] But in most cases, the Faraday pseudo-capacitor energy storage mechanism is commonly used to analyze. Harnessing the variable valence states of pseudocapacitive materials to store charges. According to the differences in the thickness of MnO_2-based electrode materials, it is further divided into two kinds of charge storage mechanisms for Faraday pseudo-capacitor. On the nanoscale MnO_2-based electrode layers for surface charge storage. The reversible faradaic reaction on/near the electrode surface can be accomplished by adsorption/desorption of ions which from electrolyte. The process is quite similar to the physical adsorption/desorption in an EDLC, and the difference is that electrochemical reactions take place in fact. It is usually expressed by eqn (1):

$$(MnO_2)_{surface} + C^+ + e^- \rightarrow (MnO_2{}^-C^+)_{surface} \quad (1)$$

In the formula, $C^+ = Li^+$, Na^+, K^+, *etc.* Since the electrolyte cations have opposite charges to the O atoms in the $[MnO_6]$ octahedron, and they are attracted to the O atoms and become electrically neutral during the charge/discharge. The additional generated charges are transferred to the nearby Mn atom, which results in the change of Mn^{4+} to Mn^{3+}.[72] Furthermore, electrolyte cations or protons can also be used for charge storage through intercalation/deintercalation in the bulk phase of MnO_2-based electrode materials.[73,74] Eqn (2) is expressed as follows:

$$MnO_2 + C^+ + e^- \rightarrow MnOOC \quad (2)$$

In the formula, $C^+ = Li^+$, Na^+, K^+, *etc.* Generally, the bulk pseudo-capacitive reaction is limited to the subsurface layer of MnO_2, with a thickness of about 420 nm according to Brousse's study.[75] Due to the thickness of the bulk MnO_2-based electrode materials, the resistance to the diffusion of electrolyte cations or protons in its interior is larger. It affects the rate of ion diffusion and charge transfer, and its conductivity is poor as well. Thus, it is further illustrated that the thickness of the MnO_2-based electrode materials is crucial to the capacitance.

4. Challenges of MnO_2-based electrode materials

4.1 Effect of active sites on capacitance

The accommodating level of MnO_2-based electrode materials for protons or cations directly determines its charge storage capacity, which affects its electrochemical performance. Generally, adjusting the size of the crystal to increase the specific surface areas is a way to obtain higher specific capacitance. For various crystal forms, the capacitance values exhibited by MnO_2-based electrode materials are significantly different, which mainly depends on the size of spaces such as tunneling or interlayer spacing in the crystal structure of different dimensions. It is found that the capacitance value decreases for different crystal forms of MnO_2, which following is the order: $\alpha > \delta > \gamma > \lambda > \beta$.[55,76] However, due to the small proportion of effective Mn atom active centers in the crystal structure, which can attract fewer negative charges. With the increase of crystal structures and particle sizes of MnO_2 of a specific phase, the electrochemical performance is reduced. Therefore, increasing the specific surface areas and exposing more effective active sites have become a necessary way to improve electrochemical performance.

4.2 Influence of intrinsic conductivity on electrochemical properties

On the other hand, electrical conductivity is also one of the important factors affecting the electrochemical performance of electrode materials. Although MnO_2-based electrode materials have fast and reversible redox reactions. Actually, the capacitance results of pure phase MnO_2 is only 14–43% of the theoretical capacity can be achieved. This phenomenon may be due to the electrons/ions transport *via* the MnO_2 electrode|electrolyte interface is relatively slow. Besides, the internal resistance is relatively large during the process of charging and discharging, which seriously reduces its rate capability.[77] The conductivity of MnO_2-based electrode materials is determined by its own inherent structural properties, which make the actual capacity far from the theoretical capacity. However, the semiconductor property can determine the internal structural properties of MnO_2, and its band gap is 0.25 eV. Therefore, to obtain better electrochemical performance, MnO_2 must reduce its band gap to favor metal characteristics. Hence, the key to improving the electrical conductivity of MnO_2-based electrode materials lies in how to improve the limited electron transfer on the surface and the interior, that is, change its electronic properties.

4.3 Effect of crystal structure on cyclic stability

Finally, the structural stability as another important factor in evaluating the performance of electrode materials to determine the cyclic stability of the materials. In all electrode materials which involving MnO_2, the unavoidable disproportionation reaction of Mn element causes the problem that Mn always dissolves slowly in the electrolyte.[78] The role of Mn atoms is to absorb excess charges, because the reduction of Mn leads to a decrease in the storage capacity of charges and affects the final cyclic stability of the materials. The size of the ions in the electrolyte and the spatial structure of the MnO_2 are not match. The crystal structure of MnO_2 expands and collapses when protons or cations are inserted or extracted, respectively. Consequently, it is urgent to improve the structural stability of MnO_2.

5. Engineering strategies to improve electrochemical performance

In view of the above challenges faced by MnO_2-based electrode materials, researchers have proposed methods such as morphology control, introduction of defects or doping of various elements, and construction of heterostructures to improve certain properties of MnO_2 to achieve the improvement of its overall electrochemical performance.

5.1 Morphology engineering

Morphology engineering is a common strategy to regulate the specific surface area of electrode materials. Larger specific surface area can be achieved by controlling the morphology of electrode materials and obtained to promote its electrochemical performance. Since the size of MnO_2 grains is inversely proportional to its electrochemical performance in a certain range, and it is of great significance to synthesize nanoscale MnO_2-based electrode materials. In the past period of time, many MnO_2-based nanomaterials with different morphologies have been studied, and they have been designed and prepared by various synthetic methods. After a large number of experiments and literature review, we have summarized the existing morphologies of MnO_2-based materials. Various forms of nanomaterials exist, including zero-dimensional (0D), 1D, 2D and 3D nanomaterials according to the spatial dimension, such as nanospheres, nanowires, nanorods, nanotubes, nanofibers, nanosheets, nanobelts, nano-urchins and nanoflowers (Fig. 4).

Well-constructed nanostructures can effectively shorten the diffusion distance of ions to the electrode surface and the transport path of electrons. For example, Singu *et al.*[79] prepared MnO_2 films grown on stainless steel substrates by using the sequential ionic layer adsorption and reaction method (SILAR). Three samples were synthesized according to the cycle numbers of SILAR. With the increase of cycle numbers, the diameter of the MnO_2 structure enlarged, which resulted in the change of nanoparticles into nanospheres (Fig. 5a–c). A thin film consisting of MnO_2 nanospheres in the form of α-MnO_2 and λ-MnO_2 co-existing was created eventually. The curves of the samples showed a typical triangular shape after charging and discharging tests when the diameter of MnO_2 nanospheres was 5–20 nm (Fig. 5d and e). It obtained specific capacitance up to 262 F g^{-1} and better capacitance retention in Na_2SO_4 solution (Fig. 5f). It could be concluded that nanoparticles with certain porosity were favorable for the diffusion of electrolyte ions. Tang *et al.*[80] obtained MnO_2 nanomaterials with different morphologies by changing the hydrothermal reaction times under the mild conditions. The results indicated that the morphology of MnO_2 nanomaterials depended on the hydrothermal time. When the time of hydrothermal heating was increased, the MnO_2 crystallinity increased gradually. And this leads to the morphology changed from the initial nanowhisker spherical to α-MnO_2 nanorods. It led to an increase in the pore volume of α-MnO_2, and the specific surface area was also changed from 89 m^2 g^{-1} to 119 m^2 g^{-1}. The better specific capacitance (152 F g^{-1} at 2.5 mA) was displayed when the hydrothermal time was 6 h, which had good cyclic stability. In a word, changing the hydrothermal time is beneficial to change the nanoparticles to a single nanorod structure with higher specific surface areas, which contributed to better entry of electrolyte ions to obtain higher capacitance. Yin *et al.*[81] reported a facile hydrothermal route for the synthesis of uniform and ultralong α-MnO_2 nanowires in a controllable redox reaction. Based on the nanomaterials obtained, it has many less porous with a size of ~3.8 nm. The current density of 1 A g^{-1} showed a specific capacitance of 180 F g^{-1}, and the capacitance retention was above 78% after 2000 cycles. α-MnO_2 nanowires with large specific surface area and small porosity shorten the diffusion paths of electrons and ions, thereby enhancing the electrochemical performance of SCs.

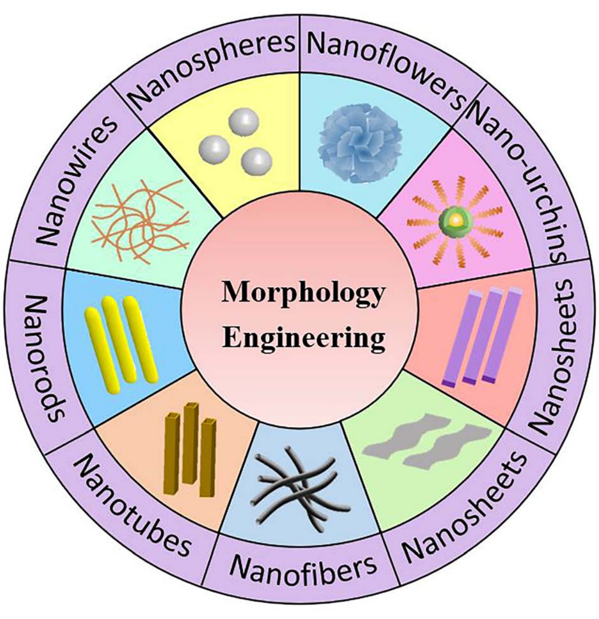

Fig. 4 Morphology engineering and structure of MnO_2-based materials.

Xu and co-workers[82] synthesize highly loose mesoporous clusters of hollow spheres and sea urchin-structured α-MnO_2 nanomaterials in a simple hydrothermal method through the "Ostwald ripening process". Among them, the shell of the hollow sea urchin was composed of densely arranged nanorods with consistent diameter and length, and the hollow sphere was composed of nanosheets. Due to its high specific surface area, it provided good cycling capability and high rate capacity. Xie *et al.*[83] developed a self-supporting material which composed of interconnected δ-MnO_2 nanosheets on graphite paper (GP). It demonstrated excellent specific capacitance (446 F g^{-1} at 1 A g^{-1}) and outstanding cyclic stability under a wide voltage window of 1.3 V. Owing to the interaction which between δ-MnO_2 and the open nanosheet structures interconnected with the GP substrates, the effective contact of the electrolyte was promoted. It increased the specific surface area and improved ion diffusion and charge transfer.

We also investigated the morphology of pure phase MnO_2 materials. MnO_2 with different morphologies was obtained by

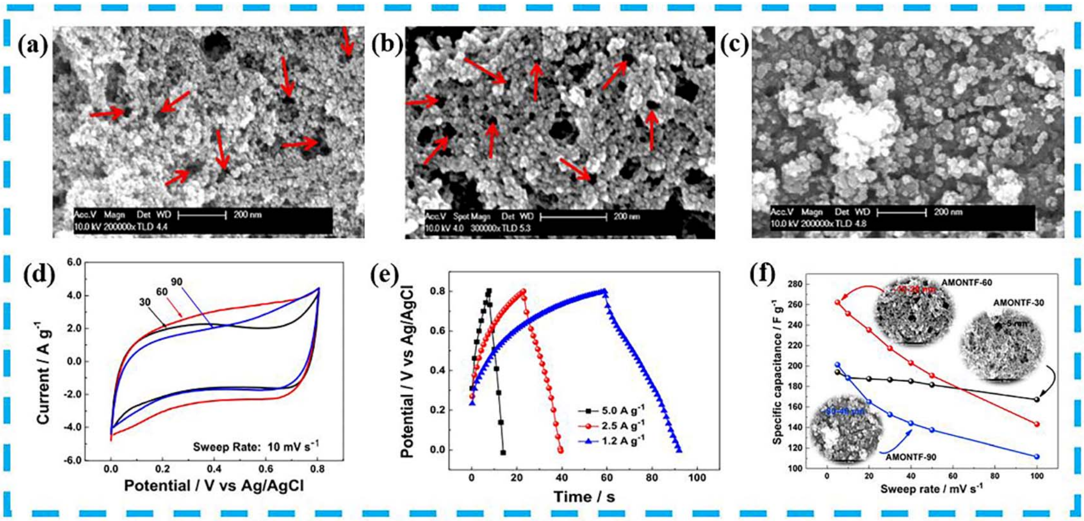

Fig. 5 Morphology of (a) sample 1, (b) sample 2 and (c) sample 3 prepared by SILAR method. (d) Comparative cyclic voltammetry (CV) of the three samples (e) The galvanostatic charge/discharge (GCD) curves of sample 2. (f) Specific capacitance of three samples with effect on scanning rate. Reproduced with permission from ref. 79. Copyright 2016, Elsevier B.V.

changing the hydrothermal temperature and reaction time under the condition of using the same precursor. For example, it was found that the obtained one-dimensional MnO_2 microparticles showed a "moss"-like uniform distribution (Fig. 6a). However, the MnO_2 samples existed in the form of "dendritic" nanorods and packed together to form clusters when both the hydrothermal temperature and time were increased (Fig. 6b and c). And its electrochemical performance was better with a specific capacitance of 257 F g^{-1} at 1 A g^{-1} when hydrothermally reacted at 160 °C for 12 h (Fig. 6d and e).

Generally speaking, the pseudo-capacitance properties of MnO_2 lead to a fast and reversible redox reaction, mainly between Mn(IV) and Mn(III). It enters protons and electrons into the lattice during the charging process, which means that the electrons released from the negative electrode enter the lattice of MnO_2 and reduce Mn^{4+} to Mn^{3+}. At the same time, the protons in the solution combine with O^{2-} in the lattice to become OH^-. Thus, for every electron and proton gained, one MnO_2 molecule is converted to MnOOH. The positive MnOOH releases H^+ to convert MnO_2. Athouël *et al.*[84] doped Mg in layered MnO_2 and investigated in depth the effect of cycling processes on the crystal structure of MnO_2 by voltammetric behavior and XRD analysis. The results show that Mg as a dopant promoted the charge transfer process and that the

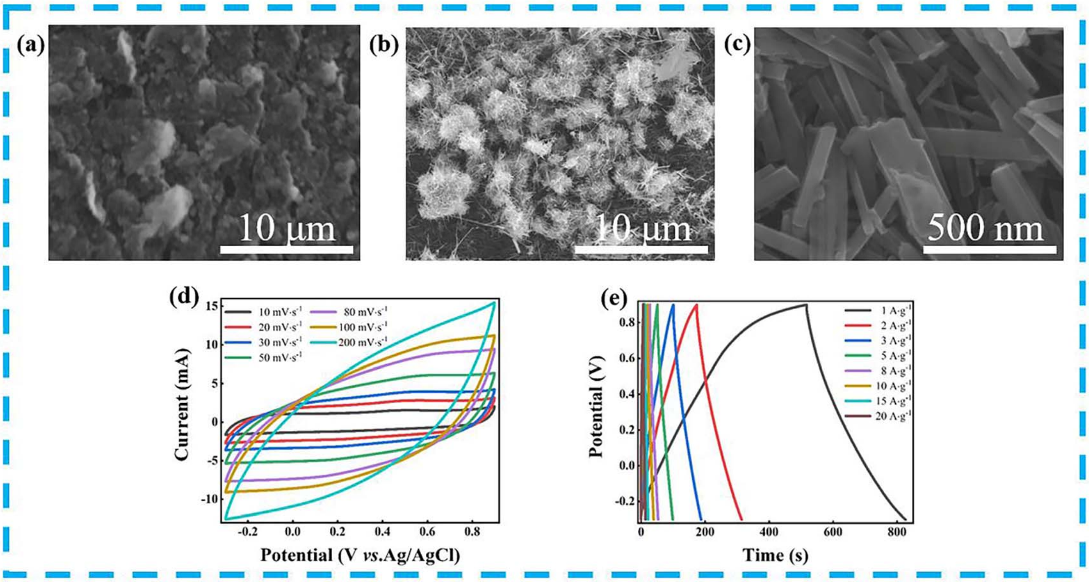

Fig. 6 SEM images of (a) sample 1 (10 μm), (b) sample 2 (10 μm) and (c) sample 2 (500 nm). (d and e) CV and GCD curves of sample 2.

charging and discharging process does not change the monoclinic structure of a classic Na-birnessite.[85] Therefore, the cycling process does not affect the crystal structure of MnO_2. The main reason for changing its structure is the size of the cations during the intercalation/deintercalation process. When the diameter of the embedded cation is smaller than its structural tunnel, the structure does not change before and after cycling. Suppose the diameter of the cation is larger than the structural tunnel. Its structure is disrupted during the intercalation of the cation into the crystal structure, resulting in an extremely rapid decrease in capacitance. In addition, the morphology of MnO_2 is more macroscopic than the valence and structure; therefore, the cycling process does not affect it significantly.

The MnO_2 structure changes fundamentally with increasing spatial dimensionality. A variety of morphologies are designed and composed, and the advantages of dimension control can be used to improve the shortcomings of one or several aspects of MnO_2-based electrode materials. Changing the morphology of electrode material, the higher porosity can be obtained to facilitate the diffusion of ions and electrons, or a larger specific surface area can be designed to expose more abundant active centers. This leads to further improvement of the electrochemical performances of MnO_2 nanomaterials in SCs.

5.2 Defect engineering

Due to the inherent internal limitations of the material, it is sometimes impossible to solve the existing problems with simple external modifications. Defect engineering is considered to be able to adjust the electronic structure of materials effectively, and the introduction of defects in MnO_2-based materials can provide them with new electronic, magnetic and optical properties.[86,87] According to the mechanism of defect formation can be grouped into interstitial defects, substitutional defects, atomic vacancies and high-dimensional defects.[88] This section focuses on common defect engineering strategies for MnO_2-based materials: (1) oxygen vacancies, (2) cation vacancies, (3) cation doping and (4) anion doping.

5.2.1 Oxygen vacancy. Oxygen vacancy (V_O) is an important defect engineering strategy that enhances electrical conductivity by using V_O as an electron donor, while utilizing the modulation of the active center state to activate the intrinsically low-valent metal center, which in turn induces the formation of a new band gap. Zhu *et al.*[89] developed a method based on solubility contrast. Taking advantage of the different solubility of inorganic salts in different solvents, δ-MnO_2 with controllable nanostructures and V_O was obtained through a simple coprecipitation process. The δ-MnO_2 had a valence state mixed with the Mn^{3+}–O–Mn^{4+} electron path after the addition of V_O, which contributed to improve electrical conductivity and electrochemical performance significantly. Through density functional theory (DFT) simulation calculations, they were found that the introduction of V_O can reduce the bond length of the Mn–O which was to effectively increase the Mn–O bond strength. After the introduction of V_O, three levels which closed to the Fermi level were generated. Compared with pristine MnO_2, the electrical conductivity was increased (Fig. 7a and b). Liu *et al.*[13] proposed a novel mechanism by utilizing self-triggered V_O for redox reactions of multiple Mn ions. An improvement in the electronic structure of MnO_2/Mn_2O_3 is achieved. It led to an abundance of V_O in the active structure inducing the new electronic states and electron redistribution between Mn and O, which resulted in a more than two-fold increase in the total charge storage. While promoting the redox reaction of multiple Mn ions (Mn^{2+}, Mn^{3+}, Mn^{4+}). The Gibbs free energy of Na^+ adsorption in the pristine MnO_2 and V_O-MnO_2 states and the density of states (DOS) of V_O-MnO_2 were calculated by DFT simulations. The simulation results showed that the adsorption energy of Na^+ on the V_O-MnO_2 surface was −3.14 eV lower than that of −2.64 eV on the intact MnO_2 surface, which further confirmed that the presence of V_O was more favorable for the transfer of Na^+. It could be imparted with a new electronic state adjacent to the Fermi level to introduce V_O in MnO_2. The electronic states could increase the carrier concentration, which improved conductivity and facilitated the transition of electrons from the valence to the conduction band by acting as a springboard. The difference in electron density for Na^+ adsorption was compared between MnO_2 without V_O and with V_O. Na^+ tended to absorb O with significant electrons, which indicated that O was the active site for Na adsorption. In particular, V_O weakened the chemical bond formed by Na and O on the surface, which promoted the adsorption/desorption of Na^+, and also provided additional adsorption sites for Na^+. It stabilized the layer structure by promoting the oxidation of Mn ions (Fig. 7c).

Recently, Zhang *et al.*[90] successfully introduced abundant V_O into the bulk MnO_2 phase by complex-induced chemical precipitation. MnO_2 with abundant bulk V_O exhibited fast charge transfer kinetics (Fig. 7d). The electronic properties of MnO_2 were investigated *via* DFT calculations, and the results showed that V_O could induce a reduction significantly in the band gap to enhance the conductivity. The concentration of V_O was proportional to the conductivity (Fig. 7e). Charge density difference calculations evidenced that electrons around O and Mn atoms were accumulated and depleted, respectively (Fig. 7f). Bader charge analysis showed that with increasing concentration of V_O, there was a greater electron transfer and a higher electron delocalization, which resulted in positive and negative region at V_O and around O, respectively. The adsorption energy of Na^+ belonged to V_O-rich MnO_2 in the electrolyte was stronger than that of MnO_2 without V_O, which proved the presence of V_O was beneficial to the storage of Na^+. The barrier of $4O_{cut}$–MnO_2 (0.10 eV) was lower than that of MnO_2 (0.29 eV) and $2O_{cut}$–MnO_2 (0.29 eV), which demonstrated that $4O_{cut}$–MnO_2 had a fast Na^+ transfer capability (Fig. 7g). At the same time, other reports had pointed out that the Mn 3d orbital state in MnO_2 with V_O was closer to the Fermi level and the state was more defined than that of MnO_2 without V_O. It was shown that V_O promoted the delocalized movement of nearby electrons to the vicinity of the low-coordinated Mn atom, causing the rapid transfer of the delocalized electrons into the conduction band and improving the overall conductivity of the system.[91] Thus, abundant bulk V_O could increase the conductivity significantly by reducing the

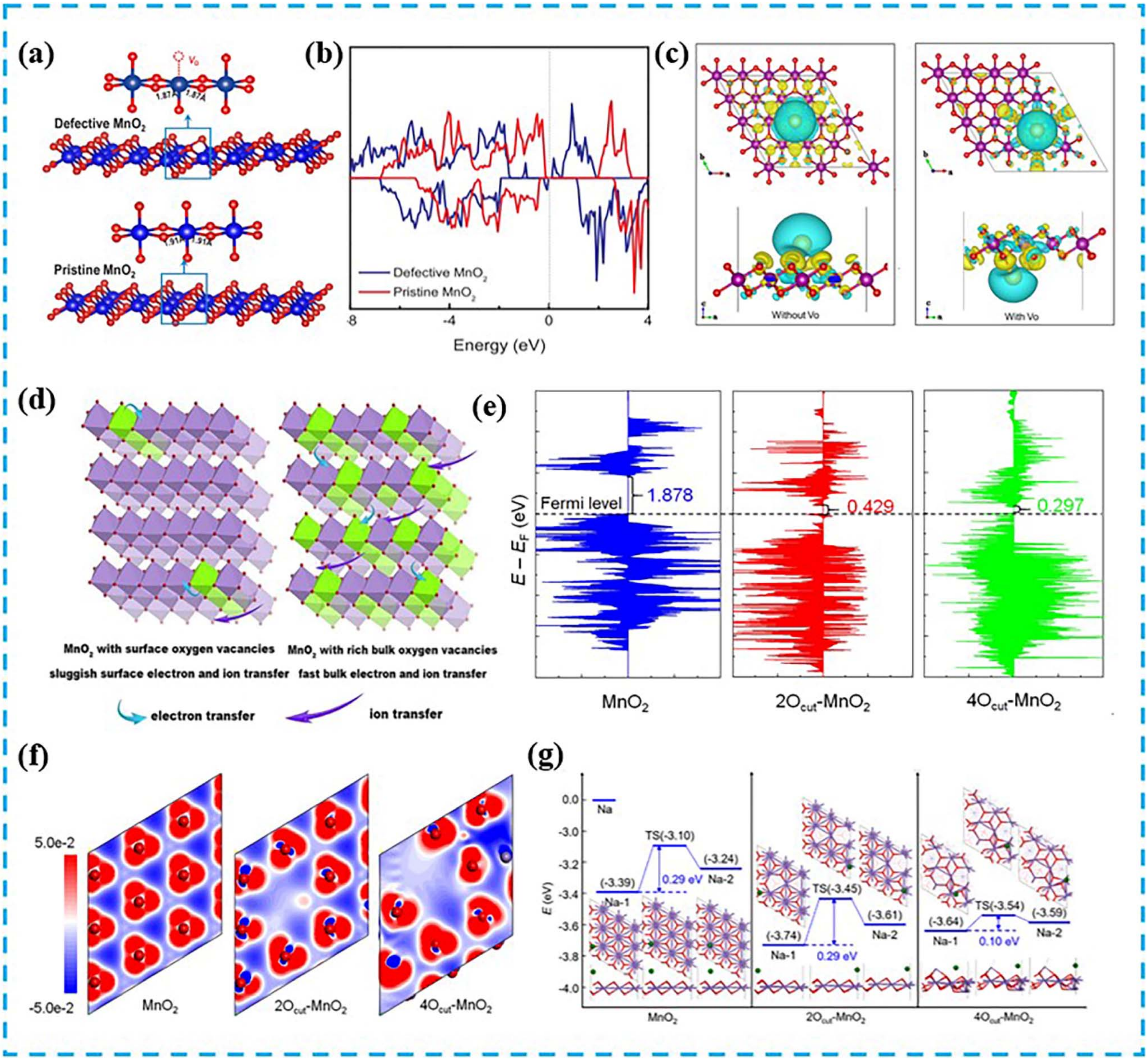

Fig. 7 (a) Constructed models of defective and perfect δ-MnO_2 surfaces. (b) Projected DOS of δ-MnO_2. Reproduced with permission from ref. 89. Copyright 2019, Elsevier Ltd. (c) Difference in electron density of MnO_2 without V_O and with V_O, blue and yellow represent charge consumption and accumulation (the Mn, O and Na atoms in purple, red and gold, respectively). Reproduced with permission from ref. 13. Copyright 2022, Elsevier B.V. (d) Charge transfer kinetics on MnO_2 with surface containing V_O and abundant bulk V_O. (e) DOS of MnO_2, $2O_{cut}$–MnO_2 and $4O_{cut}$–MnO_2 models. (f) Charge density difference between three models, with red and blue regions representing the accumulation and depletion of charge density, respectively. (g) Diagram of the energy distribution of Na^+ diffusion on three models and the related structures of the intermediate, with the potential obstacles in blue (green, purple and red represented Na, Mn and O, respectively). Reproduced with permission from ref. 90. Copyright 2021, Elsevier B.V.

band gap and increasing the electron delocalization. Furthermore, a strong local electric field was formed around V_O, which could accelerate bulk ion transfer with a low diffusion energy barrier. In order to enhance the energy storage capacity of MnO_2 effectively. Jing *et al.*[92] synthesized microsphere electrode materials using a typical hydrothermal-electrostatic self-assembly method combined with heat treatment. Based on *in situ* characterization techniques and DFT calculations, the pseudocapacitive behavior of K^+ intercalation during discharge was revealed. As the amount of K^+ intercalation increased, the length of the Mn–O bond near K^+ in the $[MnO_6]$ octahedral structure became longer, which led to a decrease in its stability. As a result, the Mn–O bond lost O and generated V_O, so that the phase transition occurred and layered MnO_2 was transformed into a stable spinel-type Mn_3O_4.

Our research group had also successfully modified MnO_2 materials by means of V_O. After the method of low temperature calcination, MnO_2 containing a certain amount of V_O was obtained by calcining at 300 °C for 4 h. In addition, the structure of CeO_2-coated MnO_2 was also formed through the additional introduction of Ce^{3+} ions. During this process, the morphology changed from nanorods to clusters formed by aggregation of nanospheres, and V_O also increased by 9.36% compared with the previous MnO_2. Therefore, the charge transfer resistance of the finally obtained material was reduced, and the electrochemical performance of the corresponding material was improved.

5.2.2 Cation vacancy. Cation vacancy can provide additional cation intercalation sites to effectively boost the charge storage capacity of transition metal oxides.[93] Thus, Mn vacancy is the only and most important cation vacancy strategy in MnO_2-based electrode materials. Wang *et al.*[94] synthesized monolayer δ-MnO_2 nanosheets with Mn vacancies by exfoliating their bulk counterparts in solution. By controlling the temperature of the prepared defect layered manganese oxide precursor, the concentration of Mn vacancies could be easily adjusted. The results showed that the lower the temperature, the more Mn vacancies were obtained. After calculations of DFT, the authors explored the implications of different types, concentrations and distributions of vacancies on the electronic structure of monolayer δ-MnO_2 nanosheets. As shown in Fig. 8a, when Mn vacancies were introduced into monolayer δ-MnO_2, it was transformed from semiconducting to semi-metallic properties due to the hybridization between the adjacent O 2p and Mn 3d orbitals around the Mn vacancies. With the increase of Mn vacancy concentration, the energy gap decreased gradually, but its semimetallic behavior was not affected. However, neither the introduction of no vacancy nor the introduction of single V_O could change the electronic properties of δ-MnO_2. In addition to using redox heat treatment to control the content of cationic defects, it could be achieved by balancing the pH to control oxides in the solution as well. Gao *et al.*[95] applied the above method to strip and re-assemble δ-MnO_2 nanosheets into 3D macroporous pseudo-capacitor electrodes with controlled Mn point defect concentration and Mn^{3+}/Mn^{4+} ratio. The defects provided two possible intercalation sites for Mn vacancies and the undercoordinated $[MnO_6]$ surface octahedron on the opposite side of the nanosheets (Fig. 8b). The decrease in pH led to an increase in the Mn^{3+}/Mn^{4+} ratio, which not only increased the concentration of Mn vacancies, but also enhanced the electrical conductivity and charge transfer efficiency due to the participation of high concentrations of Mn^{3+} in polaron hopping conduction (Fig. 8c). Meanwhile, results of electrochemical performance showed that the specific capacitance was improved from 200 F g^{-1} to more than 300 F g^{-1}, and the charge transfer resistance was also significantly reduced. Therefore, the Mn vacancies in δ-MnO_2 nanosheets increased Na^+ intercalation by providing new and low-energy intercalation sites, which enhanced cyclic stability.

5.2.3 Cationic doping. Dopants with similar ion sizes and high solubility properties can provide MnO_2-based materials with a variety of doping element choices, thereby tailoring the electrochemical properties of MnO_2-based materials according to practical applications. Doping cations (such as V, Li, Na, K, Co, Ag, La, Zn, Cu, Gd, and H) into the lattice of bulk MnO_2-based materials can release the electrochemical activity of MnO_2.[88] Cationic doping can be divided into interstitial doping and substitution doping generally. Tseng *et al.*[96] introduced Li^+, Na^+ and K^+ with different doping concentrations into α-MnO_2 nanotubes respectively, and discussed the effect of doping of several metal cations on the crystal structure of α-MnO_2. According to DFT calculations, Mn^{3+} was formed by the electron

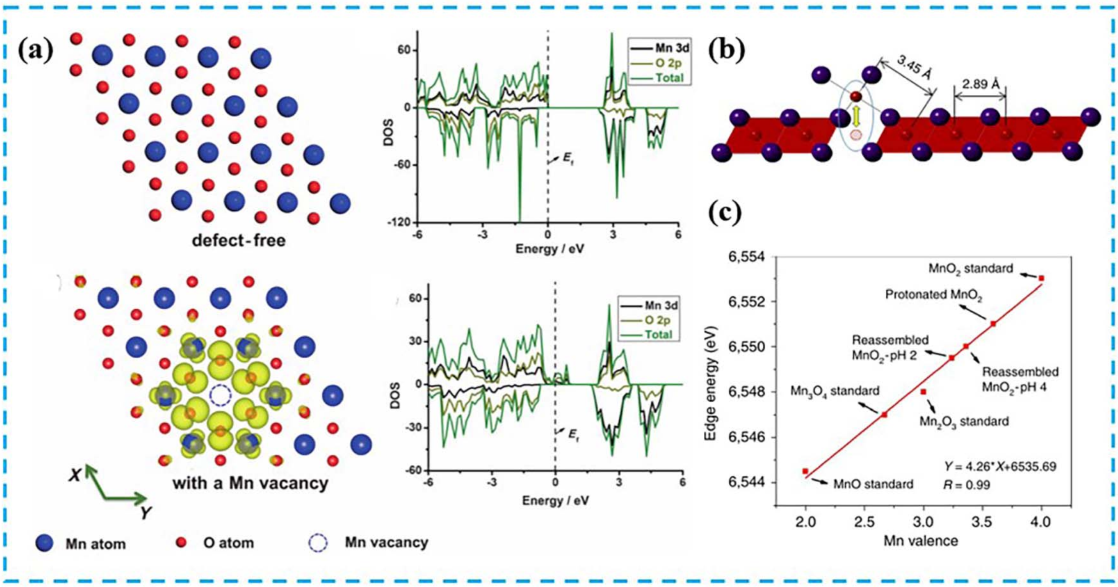

Fig. 8 (a) The charge density distribution and density of states of MnO_2 plates without Mn vacancy and with one Mn vacancy in 4 × 4. Reproduced with permission from ref. 94. Copyright 2015, Wiley-VCH. (b) Empirically estimated Mn vacancy concentration (circles) using Gaussian peak and linear baseline. (c) Average oxidation state of Mn from K-edge energies for δ-MnO_2 samples and standards obtained in different pH values. Reproduced with permission from ref. 95. Copyright 2017, Springer Nature.

transfer of K^+ doping and caused the Fermi level to overlap with the conduction band, which showed metallic behavior. The geometry did not change significantly at low K^+ doping concentration, it led to lattice expansion while at high doping concentration. The degree of expansion was proportional to the doping concentration, and the peak of the (211) plane in XRD shifted to lower 2θ values (Fig. 9a). Therefore, the doping concentration was so high that some K^+ may enter the interstitial sites, resulting in a disordered state of the structure. The significant difference in p density of state (PDOS) demonstrated that the incorporation of K^+ in the tunnel led to an enlarged *d*-spacing (Fig. 9b). And because the atomic radii of Li^+ and Na^+ were smaller than K^+, the resulting lattice spacing was smaller. The energy splitting was asymmetric due to lattice distortion, which in turn broke the Mn symmetry between the $[MnO_6]$ octahedron. Yao *et al.*[97] proposed a strategy for obtaining structural distortion of MnO_2 by doping Ni, while achieving improved electrochemical performance through fast electron and ion transfer kinetics. Ni–MnO_2 exhibited structurally distorted unit cells and expanded unit cell volume (Fig. 9c). According to the changes of Mn valence state and coordination number, it was shown that Ni doping in MnO_2 led to structural distortion in the crystal framework due to the changed of Mn–O bonds and Mn centers. At the same time, the electronic state modulation effect of electron delocalization and narrow band gap were used to enhance the conductivity. Therefore, the substitution of Mn in the octahedron by Ni not only effectively suppressed the Jahn–Teller distortion of Mn^{3+} in the structure to stabilize the MnO_2 structure and obtained excellent cyclic stability, but also provided a larger lattice parameter. It helped to lower the potential barrier of Na^+ to facilitate ion diffusion and accelerate the ion transport kinetics (Fig. 9d). In another

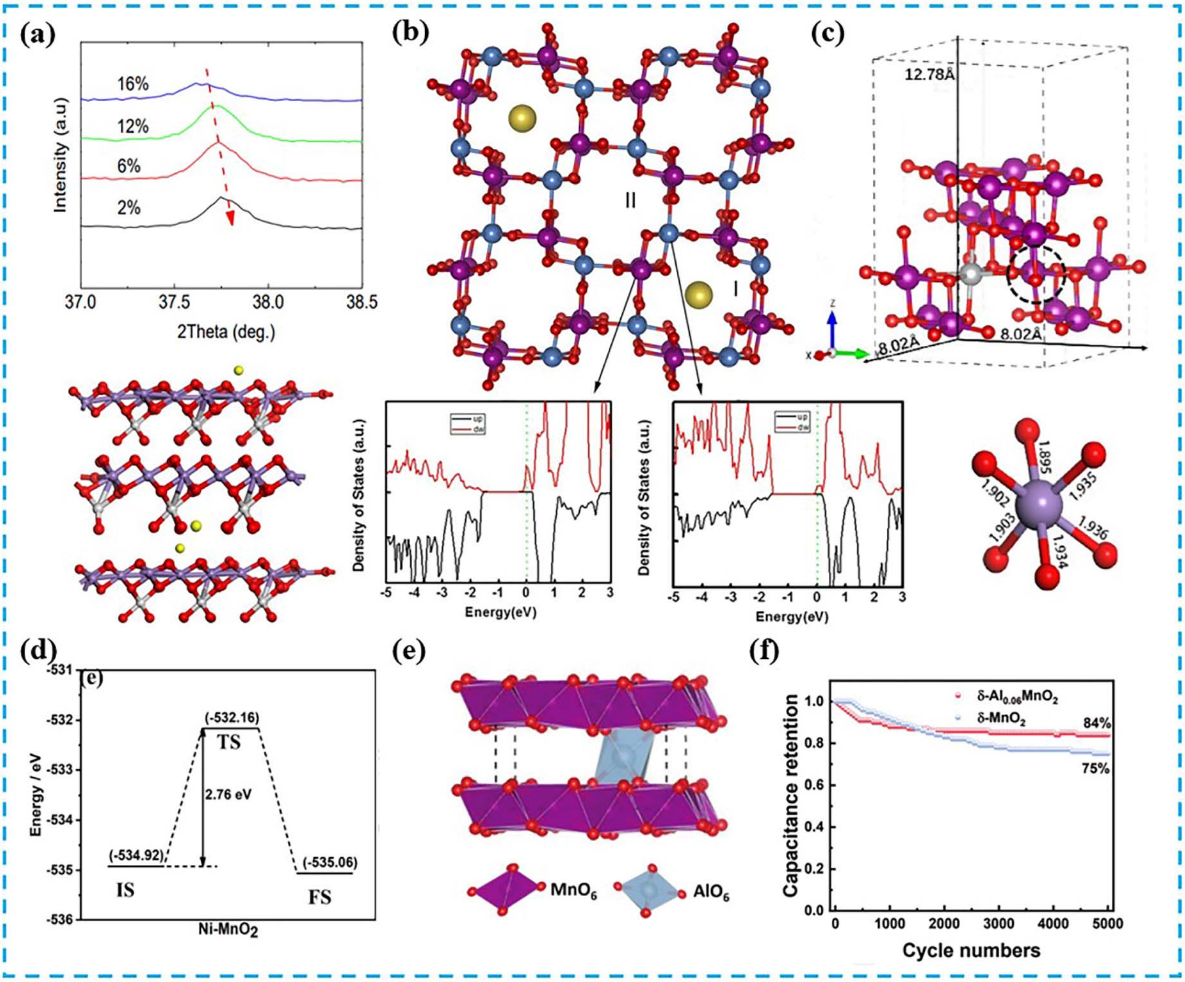

Fig. 9 (a) The magnification of the (211) crystal plane in the XRD spectra of K^+-doped MnO_2 at different doping concentrations. (b) K^+-doped two different Mn sites combined with the vertex and plane positions of the octahedral O in the MnO_2 crystal structure (blue and purple) and effects on PDOS. Reproduced with permission from ref. 96. Copyright 2015, Springer Nature. (c) The theoretically optimized structural model of Ni–MnO_2 and the magnified Mn–O bond length from the unit cell in the black circle. The purple, red and silver spheres represent the Mn, O and Ni atoms, respectively. (d) In Ni–MnO_2 illustration of Na^+ migration pathways and corresponding potential barriers. Reproduced with permission from ref. 97. Copyright 2022, Elsevier B.V. (e) The most stable structure of δ-$Al_{0.06}MnO_2$. (f) Capacitance retention of δ-MnO_2 and δ-$Al_{0.06}MnO_2$ when the current density is 10 mA cm^{-2}. Reproduced with permission from ref. 67. Copyright 2022, Royal Society of Chemistry.

example, Wan *et al.*[67] doped Al into δ-MnO_2 and obtained high specific capacitance and cyclic stability. First-principles calculations showed that the Al-doped δ-MnO_2 was mainly interstitial doping to form a stable $[AlO_6]$ octahedral structure (Fig. 9e). After Al doping, both the Mn 3d and O 2p orbitals in the valence band moved to the Fermi level, which led to the enhanced conductivity and provided more active centers for Li^+ adsorption. In addition, the substitution of Al for Mn or O atoms could suppress the surface energy and hinder side reactions or structural transitions, thus achieving better cyclic stability (Fig. 9f). Poudel *et al.*[20] synthesized Gd-doped MnO_2 by hydrothermal method. The interlayer space was widened by the doping of rare earth metal cations with large ionic radius to form a unique structure, which improved the pseudocapacitive performance of the strategy. Furthermore, the doping of a large amount of Gd could also cause defects in the crystal, thus leading to increase in surface areas and the enhancement of kinetic reversibility.

Our research group also modified MnO_2-based materials by cationic doping. We have studied a variety of cationic doping, such as Ni, Co, Ce, Bi, *etc.* Among them, Ni, Co doping and Ce, Bi doping belong to substitution doping and interstitial doping, respectively. It was found that appropriate doping was beneficial to the improvement of the electrochemical performance of MnO_2, which was consistent with the results in the literature. However, not only the performance of MnO_2 could not be improved, but also the overall test results would be affected when the doping amount was slightly larger.

5.2.4 Anionic doping. Non-metal elements, such as S, N, B, P, *etc.*, have been shown to help narrow the wide band gap of MnO_2-based materials to improve their electrochemical performance.[98] In addition, it can help the material to build a porous framework because of its low negative charge, which can be used to obtain large specific surface areas and more surface active centers for promoting contacts between active materials and the electrolytes. For example, Chi and co-workers[99] prepared B-doped MnO_2 with 3D structure by chemical reaction. According to electrochemical test analysis, B-doped electrode material had higher specific capacitance or higher active material. Due to the electron-deficient nature of B^{3+}, the concentration of OH^- on the surface of MnO_2 increased after B doping. The MnO_2 seeds formed by the disproportionation reaction between Mn^{7+} and Mn^{3+} were captured by OH^-. And when B atoms entered the lattice, the difference of B, Mn and O ion radii could easily lead to lattice distortion and dislocation. So that lattice defects reduced the interfacial energy to speed up the rate capability. Up to now, there are few defect engineering strategies for anionic doping as MnO_2-based materials in SCs. There is no sufficient mechanistic explanation, and the lack of this aspect can provide more opportunities for its further exploration.

After experiments and research, it was found that defect engineering can change the internal structure of the MnO_2 lattice to a certain extent and improve its electronic structure. Using this strategy can achieve the improvement of electronic conductivity effectively, so as to achieve the purpose of improving the electrochemical performance of MnO_2.

5.3 Heterojunction engineering

Currently, the construction of heterojunctions is one of the most common methods for developing electrode materials. Manipulate electronic structure, enhance electronic/ionic conductivity, facilitate charge transfer kinetics, build porous structures, and improve structural stability by combining with other species.[100–102] So, heterojunction engineering is also one of the most effective strategies to improve the adsorption and electrochemical performance of MnO_2-based materials. Recently, many MnO_2-based heterojunction materials for energy storage have been extensively reported.

5.3.1 MnO_2/metals. The heterojunction material has high specific capacitance and energy density as well as excellent cycling stability which formed by metal and MnO_2. It is one of the methods to obtain the best electrode materials for high-performance SCs. Surface modification/functionalization of metal nanoparticles for MnO_2-based materials can enhance the charge storage capacity. And noble metals (such as Au, Ag, Pt) can provide higher conductivity than ordinary metals.

For example, Luo *et al.*[103] utilized magnetron sputtering to synthesis the 3D network of nanofibres coated with gold on the surface. It could provide a large specific surface area and high porosity to improve the overall electrochemical performance of the material when MnO_2 was electrodeposition on the conductive networks. In another example, Khandare *et al.*[104] used gold nanoparticles to modify the surface of MnO_2 nanowires (Fig. 10a). Through surface functionalization and the increase of defects, the gold nanoparticles which decorated on MnO_2 nanowires provided good contacts for MnO_2, so that led to larger surface area and better storage capacity. The obtained cyclic stability of MnO_2 nanowires decorated with gold nanoparticles were better than MnO_2 nanowires (Fig. 10b). Deng *et al.*[47] constructed a 3D macroporous Mn core–shell structure through anodization process (Fig. 10c). Due to the high conductivity of the Mn layer, it was able to provide electron channels for charge storage and discharge (Fig. 10d). Moreover, Kumar *et al.*[44] reported the synthesis of nanoporous MnO_2–Cu structures by a facile method utilizing surface deformation and selective dealloying in the Cu–Mn system (Fig. 10e). The severe surface deformation before selective dealloying led to the *in situ* growth of nanoporous MnO_2 in the Cu-rich matrix, which enhanced the reaction kinetics. Furthermore, the nanoporous MnO_2–Cu structure provided a unique microstructure to ensure high specific surface area and small charge transfer resistance.

5.3.2 MnO_2/metal oxides. In recent years, transition metal oxides have received extensive attention because of their low price and easy availability, and they have become candidate materials for the study of electrode materials. MnO_2/metal oxide semiconductor heterojunctions, for instance, MnO_2/Mn_2O_3, MnO_2/Mn_3O_4, MnO_2/CuO, MnO_2/ZnO, MnO_2/TiO_2, MnO_2/Co_3O_4, MnO_2/MoO_3, *etc.*, have been successfully used to prepare electrode materials in SCs. Lu and co-workers[105] constructed hierarchical Mn_2O_3/MnO_2 core–shell nanofibers based on electrospinning technology (Fig. 11a). Among them, the Mn_2O_3 nanofibers provided a convenient transport path for the charge and a large number of sites for the MnO_2 core. The

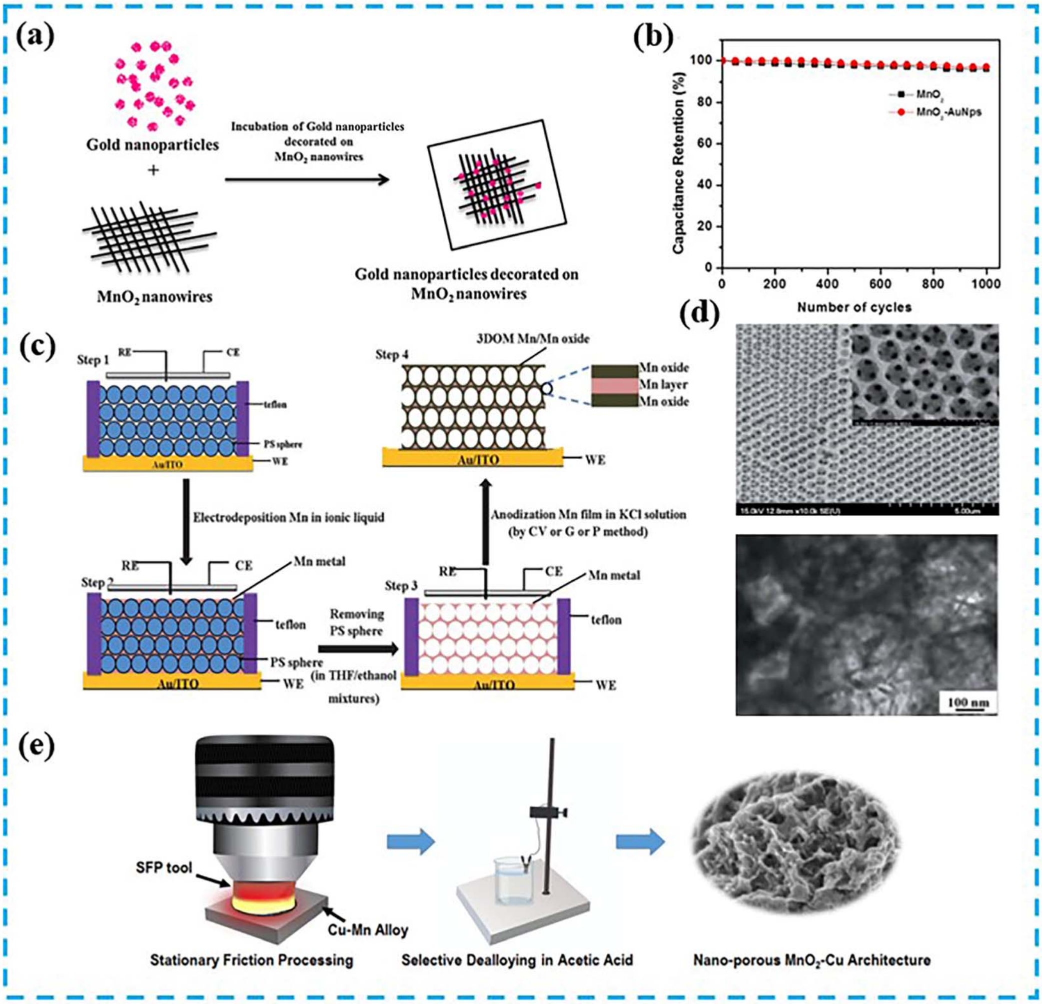

Fig. 10 (a) Illustration showing the steps in the process of MnO_2 nanowires decorated with gold nanoparticles. (b) Cyclic stability of MnO_2 nanowires decorated with gold nanoparticles. Reproduced with permission from ref. 104. Copyright 2017, Elsevier B.V. (c) Fabrication of highly porous 3D ordered macroporous Mn/Mn oxide electrodes. (d) SEM image (inset: partially enlarged) and TEM image of the inverse opal Mn with structure of 3D macro-porous. Reproduced with permission from ref. 47. Copyright 2013, Royal Society of Chemistry. (e) Development process of nanoporous MnO_2–Cu structures. The process included alloy synthesis by using an electric arc furnace, and severe surface deformation by using fixed friction machining and selective dealloying. Reproduced with permission from ref. 44. Copyright 2021, Elsevier Ltd.

formation of MnO_2 nanosheets reduced the length of the ion diffusion path and ensured the highest utilization of the material. Meanwhile, the core–shell heterogeneous structure further enhanced the Faraday redox reaction kinetics of the electrode material by increasing the specific surface area and improved the capacitive charge storage. Kang *et al.*[106] induced MnO_2 nanowires exfoliation to synthesize MnO_2/Mn_3O_4 heterojunction materials. The electrochemical performance of a single MnO_2-based electrode material was improved due to the interaction between two active materials with different structures by combining the excellent electrical conductivity of 1D α-MnO_2 nanowires with the large surface area and abundant pseudocapacitive sites provided from external Mn_3O_4. Huang *et al.*[107] combined Kirkendall growth and Ostwald ripening processes to construct a CuO/MnO_2 core–shell structure without using any surfactant (Fig. 11b). CuO nanotubes were formed by Kirkendall-type diffusion process. The interconnected MnO_2 nanosheets and hollow CuO nanotubes formed a highly porous state, which provided high surface areas and a large number of active sites for Na^+ adsorption. The unique structure consisting of MnO_2 nanosheets coated with hollow CuO nanotubes also promoted ion transport and mechanical stability. Thus, the final electrochemical properties of the material were boosted. Huang *et al.*[108] studied the structure of the hierarchical ZnO/MnO_2 core–shell as well. The combination of ZnO and MnO_2 took advantage of the small size of ZnO and its ability to act as an effective electron transport pathway. The ZnO column arrays served as conductive scaffolds so that the subsequently grown MnO_2 nanosheets could avoid conventional aggregation and ensure sufficient charge transfer. The formed MnO_2 porous ultrathin nanosheets facilitated ion diffusion and improved energy storage capacity. Rajagopal

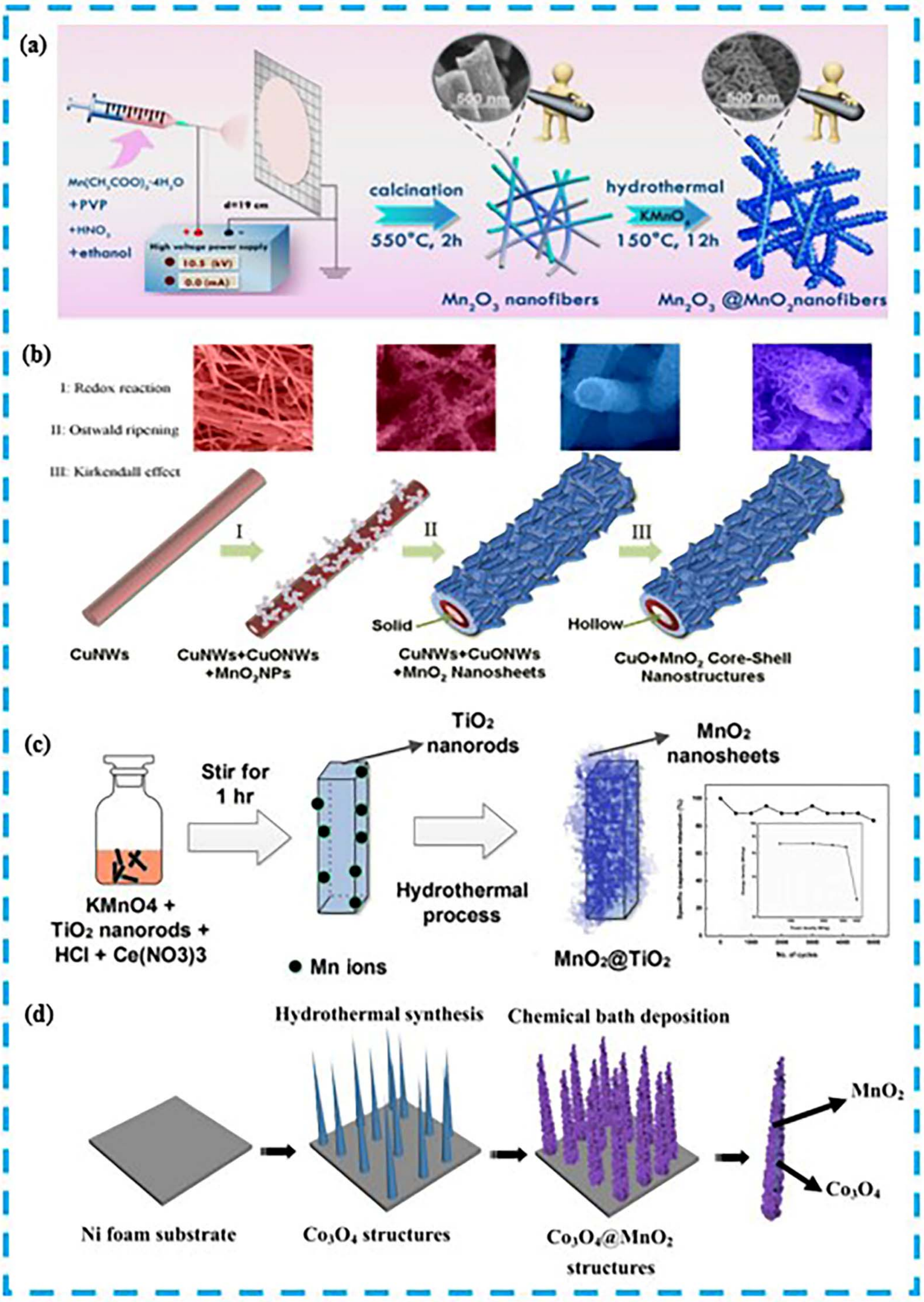

Fig. 11 (a) Diagram of the formation of Mn_2O_3/MnO_2 nanofibres. Reproduced with permission from ref. 105. Copyright 2020, American Chemical Society. (b) Schematic diagram of the growth mechanism of CuO/MnO_2 core–shell structure. Reproduced with permission from ref. 107. Copyright 2014, Springer Nature. (c) Schematic of formation TiO_2/MnO_2 core–shell structure, the inset shows the cycling stability of TiO_2/MnO_2 constructed ASC. Reproduced with permission from ref. 109. Copyright 2020, Elsevier B.V. (d) Diagram representation of the growth of 3D Co_3O_4/MnO_2 heterostructures grown on nickel foam. Reproduced with permission from ref. 111. Copyright 2016, Royal Society of Chemistry.

et al.[109] fabricated MnO_2 nanosheets packed with TiO_2 nanorods without using any template (Fig. 11c). The core–shell structured metal oxide nanocomposites provided high specific surface areas as well as excellent porosity, which was beneficial for the enhancement of electrochemical energy storage. The constructed asymmetric supercapacitors (ASCs) also showed good cycling stability. Nevertheless, Cao *et al.*[110] changed the carrier concentration in TiO_2 by hydrogenation to improve its conductivity. Similar to the above-mentioned structural composition, the synthesized ultrathin MnO_2 coatings were covered on hydrogenated TiO_2 as the core to acquire MnO_2/H–TiO_2 materials with high capacitance and high cycling stability. Zheng *et al.*[111] prepared 3D Co_3O_4/MnO_2 heterostructures on flexible substrates (Fig. 11d). The layered structure of MnO_2 nanosheets provided large surface areas for fast ion diffusion and close electrode/electrolyte contact. This not only increased the effective pathway for ion and electron transport, but also strengthened the electrochemical behavior of the material. Furthermore, similar structural and electrochemical results could be obtained by using other methods.[112] Shafi *et al.*[113] synthesized α-MnO_2/h-MoO_3 composites for the first time. The h-MoO_3 nanocrystals were presented as rods which surrounded by MnO_2 fiber structures consisting of needles. The ionic and electronic conductivity of the composites was enhanced by the heterogeneous structure formed by the tight bonding between the MnO_2 and MoO_3 nanorods. While MnO_2 provided large surface areas for adsorption and intercalation of charged ions to greatly enhance the electrochemical performance of the material.

5.3.3 MnO_2/carbon materials. MnO_2-based nanomaterials have interesting structural and transport properties, but they have a serious barrier in electrode applications because of their poor electrical conductivity formed by their own electronic structure. Carbon materials are able to provide high power density and electrochemical stability. Composites with heterogeneous structures which prepared from carbon materials with MnO_2-based nanomaterials can overcome the drawback of poor electrical conductivity of MnO_2. Graphene as one of the 2D nanostructures of carbon materials is a monolayer material consisting of carbon atoms wrapped in a two-dimensional honeycomb sp^2 carbon lattice.[114] It has many advantages, such as lager specific surface area and volume ratio, excellent electron transport properties, and chemical stability.[115] Jangu *et al.*[116] synthesized a unique V-shaped MnO_2/rGO material by a microwave-assisted hydrothermal method in a mildly acidic environment. It was found that the acetic acid concentration played an important role in the control of the V-shaped MnO_2 nanorod morphology (Fig. 12a). The V-shaped nanostructures

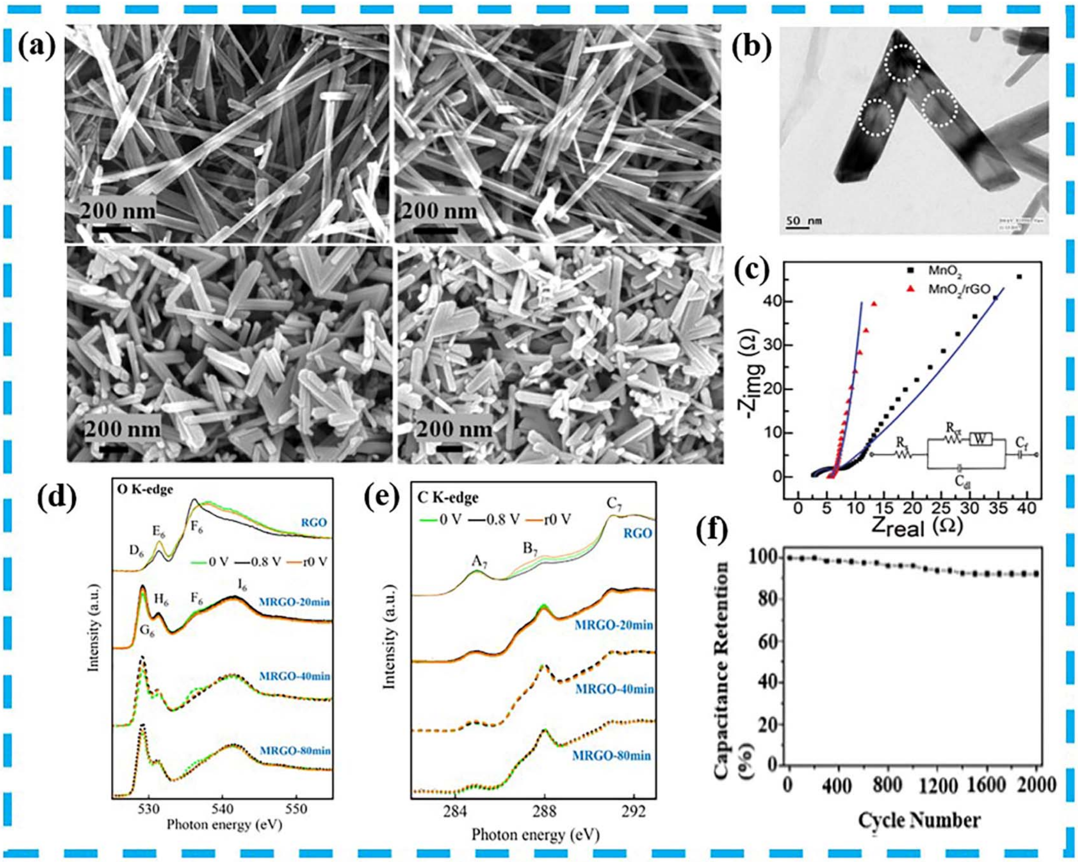

Fig. 12 (a) FESEM images of α-MnO_2 synthesized with different concentrations of acetic acid. (b) SEM image of V-shaped MnO_2 nanorods. (c) Energy quist plots for the comparison of MnO_2 and MnO_2/rGO in the frequency range of 0.01 Hz to 0.1 MHz. Reproduced with permission from ref. 116. Copyright 2021, Royal Society of Chemistry. (d) *Ex situ* XAS at the O K-edge of RGO and MRGO at different times under sequential application of potentials of 0, 0.8 and r0 V. (e) *Ex situ* XAS at C K-edges of RGO and MRGO at different times under sequential application of potentials of 0, 0.8 and r0 V. Reproduced with permission from ref. 117. Copyright 2022, Elsevier B.V. (f) Cyclic stability of the electrode at a current density of 0.2 A g^{-1} for GCD. Reproduced with permission from ref. 118. Copyright 2020, AIP Publishing.

provided more space, which is beneficial for the electrolyte ions to diffuse (Fig. 12b). The existence of rGO reduced the charge transfer resistance in Fig. 12c. Chang *et al.*[117] conducted a more in-depth study on the capacitive properties and electronic structure of MnO_2/rGO (MRGO) materials by means of electrochemistry and X-ray absorption spectroscopy (XAS). Electrochemical results indicated that the specific capacitances of RGO and MRGO were the result of the combined action of EDLC and pseudo-capacitance. The XAS results demonstrated that the contribution of the RGO contrast capacitance involved the pseudo-capacitance and the related contribution of the O function in the EDLC (Fig. 12d and e). However, compared with pristine graphene, its electrical conductivity and cycling stability were lower due to the abundant topological defects of hydrophobic rGO sheets.[49] Thus, Bai *et al.*[118] synthesized 3D graphene/MnO_2 composites *in situ* by a combination of

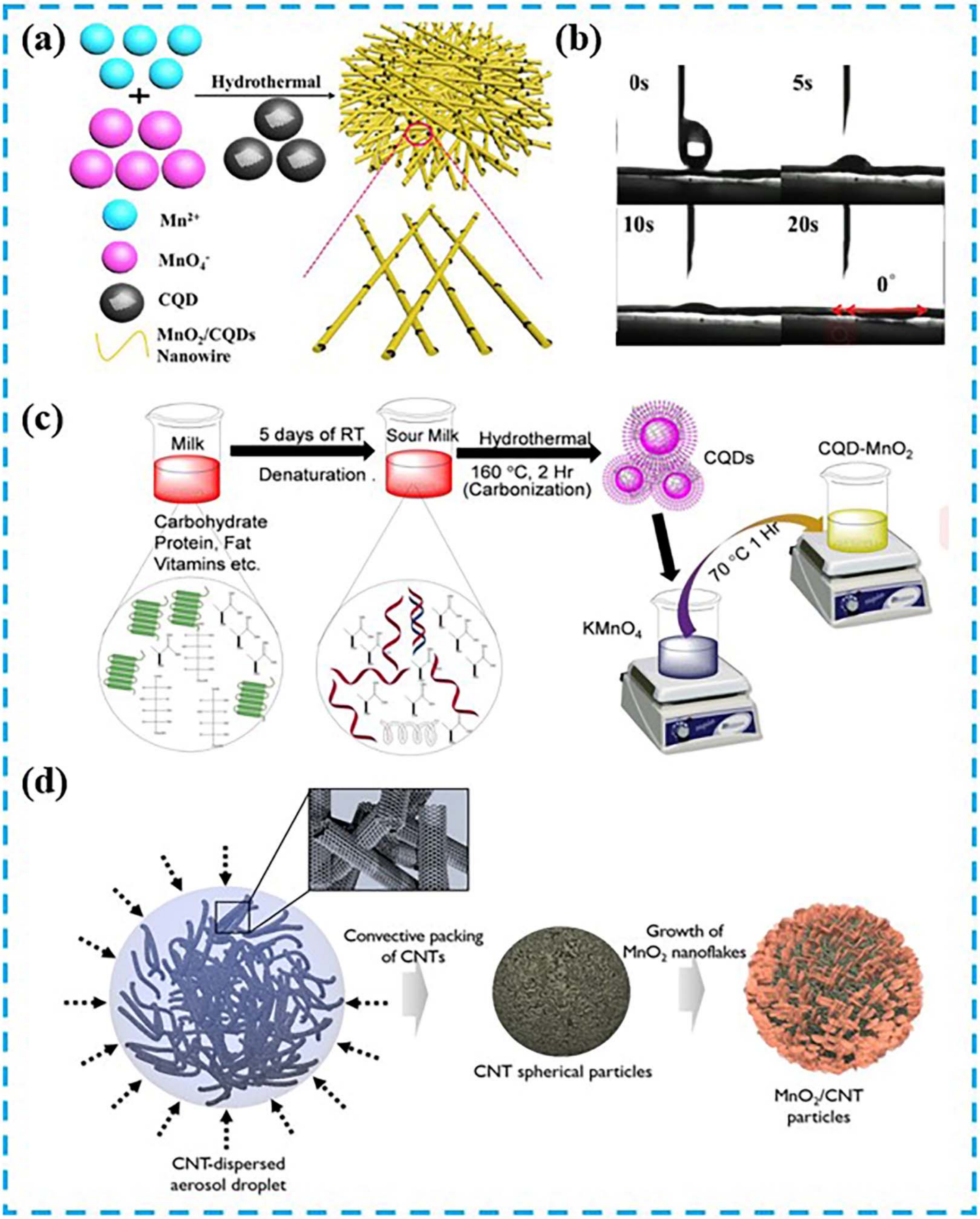

Fig. 13 (a) Schematic diagram of the fabrication process of CQD-induced MnO_2 nanowires composite films. (b) Images of CQD/MnO_2 composite film and the shape of water droplets on the film at 0, 5, 10 and 20 s, respectively. Reproduced with permission from ref. 120. Copyright 2017, American Chemical Society. (c) Schematic representation of the synthesis of CQD and CQD/MnO_2 nanohybrid materials. Reproduced with permission from ref. 121. Copyright 2018, Wiley-VCH. (d) Preparation diagram of CNT/MnO_2 core–shell particles. Reproduced with permission from ref. 123. Copyright 2017, American Chemical Society.

chemical vapor deposition and hydrothermal methods. The porous structure of 3D conducting graphene foam provided space for the rapid movement of electrolyte ions on the MnO_2 surface. The MnO_2 nanoflowers not only effectively restrained the collapse of pores in 3D graphene foam, but also formed layered structures that shortened the ion diffusion paths as well as enhancing the cyclic stability of the material (Fig. 12f).

Carbon Quantum Dots (CQDs) are considered as promising active nanomaterials due to their unique specific surface area, good water dispersibility and electrical conductivity.[119] CQDs exhibit excellent electrochemical performance when combined with pseudocapacitive materials. Lv *et al.*[120] fabricated ultralong MnO_2 nanowires *via* a CQD-induced process (Fig. 13a). The formed CQD/MnO_2 films exhibited superhydrophilicity in aqueous solution, which significantly improved the wettability between electrode and electrolyte (Fig. 13b). The obtained electrode material showed high specific capacitance, good reversibility and good stability. Prasath *et al.*[121] prepared CQDs-coated MnO_2 nanostructures by using waste yogurt (Fig. 13c). It had excellent electrochemical performance due to its excellent electrical conductivity, extremely small size and carrying a variety of functional groups on its surface. In addition, carbon nanotubes (CNTs) also had higher electrical conductivity and controllable specific surface areas. Li *et al.*[122] prepared 3D CNTs by large-area ultrasonic spraying of the surface, and the 3D CNTs provided sufficient sites for MnO_2 nanoparticles. High specific capacitance and good cycling stability were obtained through the good dispersion of MnO_2 on the CNTs surface. Gueon and co-workers[123] synthesized core–shell structures of CNTs coated with MnO_2 nanosheets (Fig. 13d). Because of the stronger binding of MnO_2 nanosheets on the CNT surface, this led to their low interfacial resistance. And the radial growth of MnO_2 nanosheets made the existence of radial spaces between the layers on the spherical CNTs particles, which enhanced the ion diffusion to obtain high capacitive performance (370 F g^{-1} at 0.5 A g^{-1}). Activated carbon (AC) is also commonly used for hybridization with transition metal oxides. Choi *et al.*[24] used a simple hydrothermal method to synthesize AC/MnO_2 composites with different mass ratios. The study found that the addition of MnO_2 could improve the electrochemical performance of AC within a certain range. However, with the increase of MnO_2 addition led to the decrease of porosity, which further made the electrochemical performance of the composites decreased.

5.3.4 MnO_2/others. We have summarized other MnO_2-based materials containing heterojunctions, as shown in Fig. 14. It can also be used to prepare interfacial structures, modify electronic structures, functionalize active sites and provide additional functionality.

Zhao *et al.*[124] prepared MnO_2/carbon nano-support sheet (CNS) arrays *via* Mn-MOF-derived CNS nanosheets (Fig. 15a). The pristine framework of Mn-MOF not only provided a path for fast electron transport and enhanced electrical conductivity. The *in situ* formed MnO_2 nanosheet arrays and the derived carbon nanosheets also generated strong coupling, so the final electrode material achieved excellent capacitance and cyclic stability. Chen *et al.*[125] *via* Fe_2O_3 derived from MIL-88A as a core and surface-modified it with an array of vertically grown MnO_2 nanosheets. The as-synthesized Fe_2O_3@MnO_2 material provided a sufficient interface for electrode–electrolyte contact due to the modification of nanosheet arrays. The large pore volume also provided portability for rapid ion diffusion, so it exhibited good capacitive performance (908.5 F g^{-1} at 1 A g^{-1}) and cyclic stability. Fu *et al.*[126] prepared core/sheath structured MnO_x/PPy nanowires *via in situ* polymerization of polypyrrole (PPy) (Fig. 15b). Conductive V_O was introduced into MnO_x simultaneously during the formation of the PPy sheath. And the mesoporous PPy nanoparticles were used to form chemical bonds with their underlying layers to promote electron transfer and restraint the dissolution of Mn. Liu *et al.*[127] obtained MnO_2 nanosheet structures enriched with 3D mesopores interconnected with polyaniline (PANI) chains, which underwent

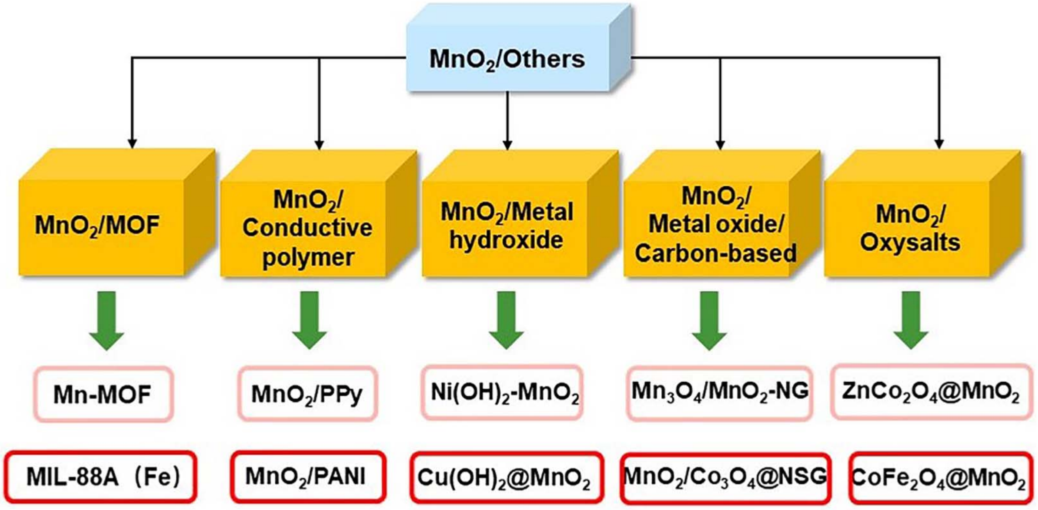

Fig. 14 Recently reported heterogeneous junctions of MnO_2-based electrode materials with other substances.

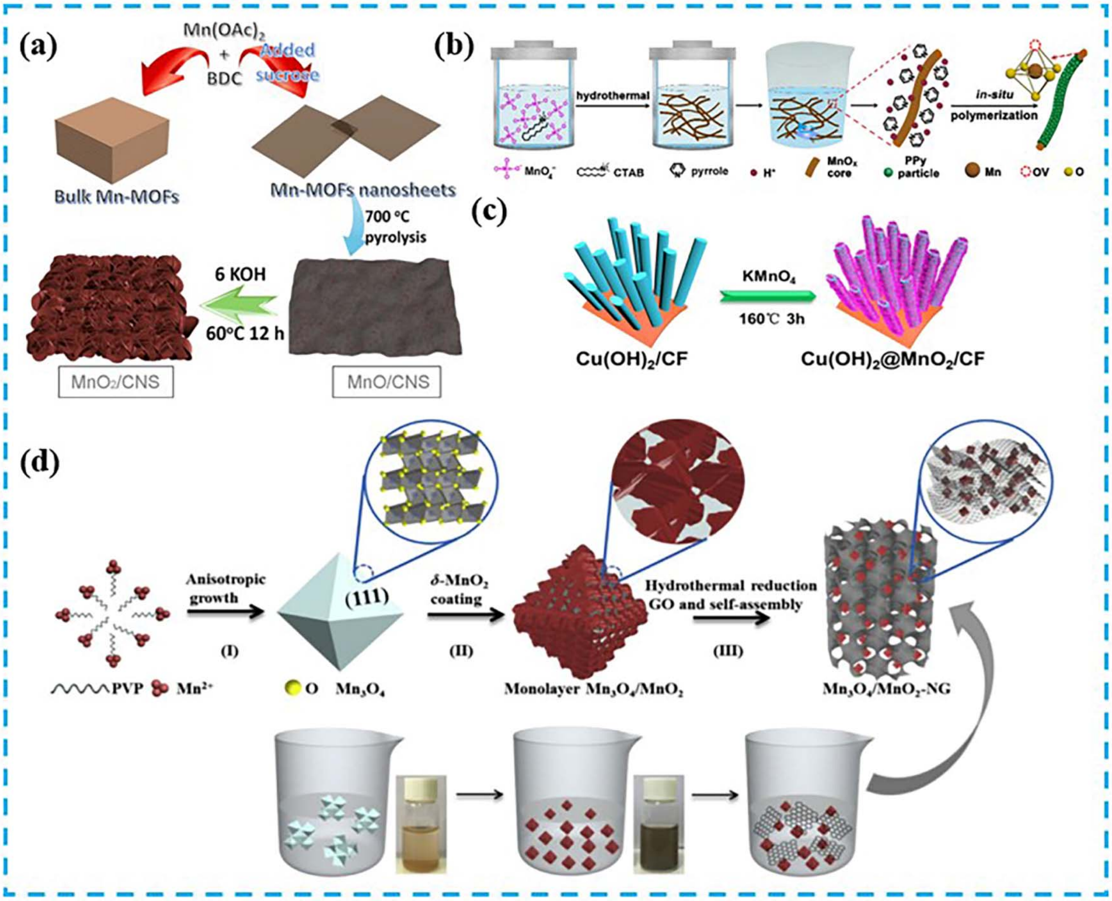

Fig. 15 (a) Schematic diagram of the preparation of vertically aligned MnO_2 nanosheets strongly coupled with carbon nanosheets. Reproduced with permission from ref. 124. Copyright 2018, Springer Nature. (b) Illustrative diagram of the formation of MnO_x/PPy nanowires. Reproduced with permission from ref. 126. Copyright 2019, Elsevier Inc. (c) Schematic diagram of the synthesis of $Cu(OH)_2$@MnO_2/CF nanorod arrays. Reproduced with permission from ref. 129. Copyright 2019, Elsevier Inc. (d) Synthesis in process of Mn_3O_4/MnO_2–NG and schematic representation of the specific nanostructures of Mn_3O_4 octahedral, as well as Mn_3O_4/MnO_2 particles and Mn_3O_4/MnO_2–NG. Reproduced with permission from ref. 130. Copyright 2018, Elsevier B.V.

a fast chemical oxidation polymerization reaction by electrostatically grafting the negatively charged surface of MnO_2 with aniline monomers. Due to the exposure of the reaction center on the electrode surface and the porous structure formed by the combination of PANI chains, it could be used for electron transport and ion diffusion pathway shortening. Li *et al.*[128] synthesized $Ni(OH)_2$–MnO_2 hierarchical nanosheet arrays. The formed heterostructure provided lattice fringe distortion as additional active centers, which combined the synergistic effect of the two to improve the capacitive performance (area capacitance of 14.7 F cm^{-2} at 2.5 mA cm^{-2}) of the material. Wang *et al.*[129] synthesized $Cu(OH)_2$@MnO_2 core–shell nanorod arrays on a copper foam substrate (Fig. 15c). The 1D $Cu(OH)_2$ nanocrystalline nuclei provided a scaffold for MnO_2 nanosheets growth and facilitated the ions and electrons to diffuse rapidly. The 2D MnO_2 nanosheets used as the shell provided a great deal of active sites. Cui *et al.*[130] reported novel Mn_3O_4/MnO_2–NG hierarchical nanostructures (Fig. 15d). The 3D conductive network of NG provided an open path for electron/ion transport while being in close contact with Mn_3O_4/MnO_2. The enhanced conductivity also increased the synergy of the components, which promoted the electrode reaction kinetics. Adaikalam *et al.*[131] improved the problems of poor reversibility and stability in the presence of single MnO_2 and Co_3O_4 electrodes by N and S double doped GO sheets. The overall mechanical strength and electrical conductivity of the material was also enhanced and allowed more ion penetration into the electrode. Hybridization of MnO_2-based materials with oxygenates could enhance the electrochemical performance through their structural advantages. Gao *et al.*[132] designed unique $CoFe_2O_4$@MnO_2 nanoarrays based on nickel foam. The porous framework formed by $CoFe_2O_4$ contributed sites for the growth of MnO_2, which promoted the enhancement of electronic/ionic conductivity. Jia *et al.*[133] prepared $ZnCo_2O_4$@MnO_2 core–shell structure in which the generation of MnO_2 films could provide large specific surface areas to efficiently promote the rapid ion transport. The final result is reflected in the assembled ASC devices. Therefore, it shows different MnO_2-based materials glowing LEDs for heterojunction engineering in Fig. 16.

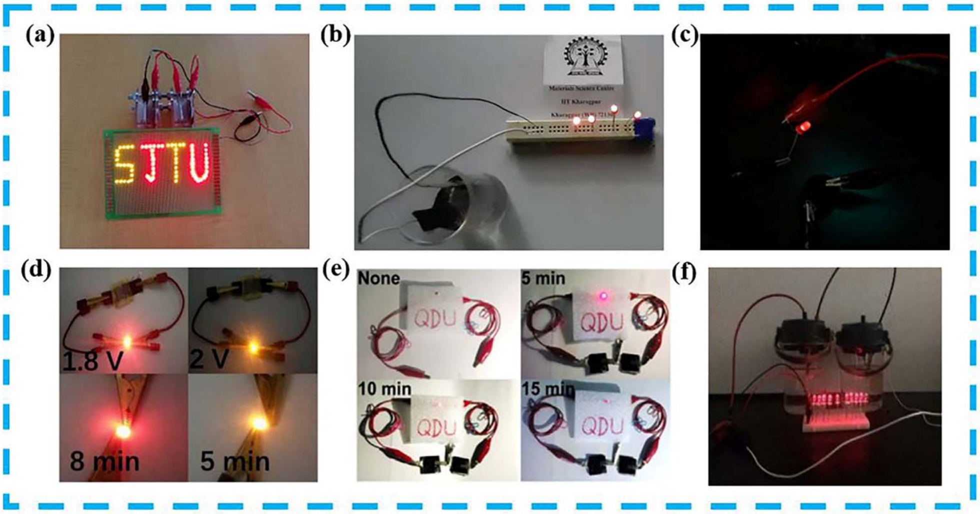

Fig. 16 (a) Device of Ar-plasma treated α-MnO_2 nanowires in two series powered 65 LEDs. Reproduced with permission from ref. 134. Copyright 2018, Elsevier B.V. (b) The V-shaped MnO_2 powers four LEDs after charging. Reproduced with permission from ref. 116. Copyright 2021, Royal Society of Chemistry. (c) Digital image of a red LED lit by the ASC composed of MnO_2/CNT. Reproduced with permission from ref. 123. Copyright 2017, American Chemical Society. (d) A red and a yellow LED illuminated by the single device of hierarchical MnO_2–Mn_3O_4. Reproduced with permission from ref. 106. Copyright 2019, Elsevier Ltd. (e) Photographic images of two solid-state ASCs made of $Cu(OH)_2$@MnO_2/CF in series lighting a red LED bulb. Reproduced with permission from ref. 129. Copyright 2019, Elsevier Inc. (f) A digital image showing the two devices composed of $CoFe_2O_4$@MnO_2 in series can lighten up ten red LED indicators. Reproduced with permission from ref. 132. Copyright 2017, Elsevier Ltd.

The systematically summarizes the adjustment of the electrochemical properties of MnO_2-based electrode materials by different engineering strategies, and shows the differences of each strategy in Table 2. Overall, the results obtained are still far from the theoretical requirements.

6. Summary and perspectives

MnO_2 is a potential electrode material in both crystal structure control and energy storage. In this review, we give a systematic description of various strategies based on MnO_2-based electrode materials through morphology engineering, defect engineering and heterojunction engineering. Many strategies are used to prepare MnO_2-based electrode materials to improve their electrochemical properties. However, there are still problems that deserve our attention, whether using strategies such as morphology engineering or defect engineering, which are only matter of fact, all lacking a systematic process and mechanism analysis of a single strategy. As a conclusion, MnO_2-based electrode materials still have numerous difficulties to overcome, while leaving some space for more in-depth exploration (Fig. 17).

The following are issues that may need to be solved immediately:

(1) The morphology engineering based on MnO_2 nanostructures can be used to influence the final electrochemical performance by means of extrinsic modification. For example, increasing specific surface area and exposing effective active sites, shortening ion diffusion paths and electron transport distances, and promoting charge transfer and accelerating reaction kinetics.[81–83] At present, a large number of synthetic methods on the morphology and porous structure of MnO_2 have been developed to enhance its electrochemical behavior. Most studies are limited to the same dimension, and they lack systematic studies on the formation of MnO_2 porous structure in multi-dimensional space. In the process of electrochemical reaction, the existence of disproportionation reaction will lead to the reduction of specific surface area or the reduction of effective active sites in the MnO_2 structure. Moreover, the more complex structure of MnO_2 also requires a complete set of theories to describe the surface reaction mechanisms corresponding to different morphologies. Therefore, this type of research is relatively lacking, and new methods need to be explored to obtain structures with excellent properties and certain stability. We should focus on the reports which related to new technologies and methods to stabilize the morphology and structure of MnO_2. In addition, it is quite difficult to obtain high-purity crystalline MnO_2, and it is urgent to develop new strategies to prepare single-phase MnO_2 materials.

(2) Defect engineering can adjust the electronic structure of MnO_2-based materials effectively according to the formation mechanisms of different defects. For instance, oxygen vacancy can change the bond length by adjusting the state of the active centers. And cation vacancies can provide additional intercalation sites to enhance the storage capacitance. Besides, cationic doping and anionic doping can use positive and negative charge attraction and different positions in the lattice to change the structure band gap, thereby enhancing conductivity and releasing electrochemical activity.[88,89,93,98] There are few reports on anionic doping as MnO_2-based electrode materials, so that

Table 2 Differences in electrochemical performance of MnO_2-based electrode materials displayed by different engineering strategies

Strategy	Active materials	Cycle stability	Specific capacitance	Electrolyte	Rate stability	Ref.
Morphology engineering	MnO_2 nanospheres thin films	72.3% (after 1000 cycles)	206.2 F g^{-1} at 1.25 A g^{-1}	1 M Na_2SO_4	75.8% (1.25 to 5 A g^{-1})	71
	α-MnO_2 nanorods	87% (after 100 cycles)	152 F g^{-1} at 2.5 mA	1 M Na_2SO_4	75% (2.5 to 10 mA)	72
	α-MnO_2 nanowires	78% (after 2000 cycles)	180 F g^{-1} at 1 A g^{-1}	1 M Na_2SO_4	40% (1 to 8 A g^{-1})	73
	α-MnO_2 hollow spheres and hollow urchins	89% (after 350 cycles)	167 F g^{-1} at 2.5 mA	1 M Na_2SO_4	74.3% (2.5 to 10 mA)	74
	δ-MnO_2/GP	87.2% (after 30 000 cycles)	446.6 F g^{-1} at 1 A g^{-1}	1 M $NaNO_3$	66.8% (1 to 10 A g^{-1})	75
Defect engineering	Defective MnO_2	89.4% (after 4000 cycles)	202 F g^{-1} at 1 A g^{-1}	1 M Na_2SO_4	NA	79
	MnO_2–C	83.9% (after 10 000 cycles)	286.9 F g^{-1} at 1 A g^{-1}	1 M Na_2SO_4	78.4% (1 to 20 A g^{-1})	80
	2D birnessite δ-MnO_2	84.7% (after 5000 cycles)	382 F g^{-1} at 5 mV s^{-1}	1 M KOH	67.4% (1 to 8 A g^{-1})	81
	MnO_x@rGO microspheres	90% (after 10 000 cycles)	405 F g^{-1} at 1 A g^{-1}	6 M KOH	76.5% (1 to 20 A g^{-1})	82
	δ-MnO_2 nanosheets	83% (after 1000 cycles)	306 F g^{-1} at 0.2 A g^{-1}	1 M Na_2SO_4	NA	87
	Ni–MnO_2	85% (after 10 000 cycles)	379 F g^{-1} at 1 A g^{-1}	1 M Na_2SO_4	74.1% (1 to 20 A g^{-1})	89
	Al doped δ-MnO_2	84% (after 5000 cycles)	450 mF cm^{-2} at 0.1 mA cm^{-2}	1 M Li_2SO_4	77.8% (0.1 to 2 mA cm^{-2})	90
	GdMnO_2/$Ni(OH)_2$ nanorods	108.3% (after 10 000 cycles)	118.61 mA h g^{-1} at 1 A g^{-1}	2 M KOH	57.5% (1 to 10 A g^{-1})	20
	B doped MnO_2 film	NA	269 F g^{-1} at 50 mV s^{-1}	0.5 M Na_2SO_4	58.7% (2 to 500 mV s^{-1})	92
Heterojunction engineering	Au–MnO_2 nanowires	97% (after 1000 cycles)	249 F g^{-1} at 1 mV s^{-1}	1 M Na_2SO_4	65.9% (1 to 5 mV s^{-1})	96
	Nano-porous MnO_2–Cu architecture	95% (after 4000 cycles)	2.8 F cm^{-2} at 5 mA cm^{-2}	1 M Na_2SO_4	35.7% (5 to 25 mA cm^{-2})	97
	Mn_2O_3@MnO_2 core–shell nanofibers	86.5% (after 5000 cycles)	225 F g^{-1} at 0.2 A g^{-1}	1 M Na_2SO_4	39.8% (0.1 to 10 A g^{-1})	98
	Hierarchical MnO_2–Mn_3O_4	99.3% (after 5000 cycles)	406.2 F g^{-1} at 1 A g^{-1}	1 M Na_2SO_4	68.8% (1 to 20 A g^{-1})	99
	Nanoflakes MnO_2/rGO	99.4% (after 5000 cycles)	482.4 F g^{-1} at 10 mV s^{-1}	1 M Na_2SO_4	NA	100
	3D-graphene/MnO_2 foam	92.2% (after 2000 cycles)	333.4 F g^{-1} at 0.2 A g^{-1}	1 M Na_2SO_4	NA	111
	CQD–MnO_2	100% (after 1200 cycles)	189 F g^{-1} at 0.14 A g^{-1}	1 M Na_2SO_4	34.4% (0.14 to 2 A g^{-1})	114
	MnO_2/CNS nanosheet arrays	96.1% (after 5000 cycles)	339 F g^{-1} at 0.5 A g^{-1}	1 M Na_2SO_4	53.8% (0.5 to 2 A g^{-1})	117
	MnO_x/PPy nanowires core/sheath structure	97.4% (after 10 000 cycles)	1091.4 F g^{-1} at 1 A g^{-1}	1 M Na_2SO_4	81.6% (1 to 20 A g^{-1})	119
	$Cu(OH)_2$@MnO_2/CF core–shell nanorods array	85.17% (after 5000 cycles)	708.6 mF cm^{-2} at 2 mA cm^{-2}	6 M KOH	74.65% (2 to 20 mA cm^{-2})	122
	MnO_2/Co_3O_4 with N and S co-doped GO	95% (after 10 000 cycles)	614 F g^{-1} at 1 A g^{-1}	6 M KOH	57% (1 to 30 A g^{-1})	124

the reaction mechanism of electrode materials in electrolyte is not perfect. Therefore, it is necessary to expand the research scope of anions to deeply understand and explore them in this regard.

(3) The construction of MnO_2-based heterojunction materials is one of the most effective strategies to enhance the electrochemical performance. The electronic structure is regulated by the interaction generated by binding with other substances, promoting the charge transfer kinetics, building

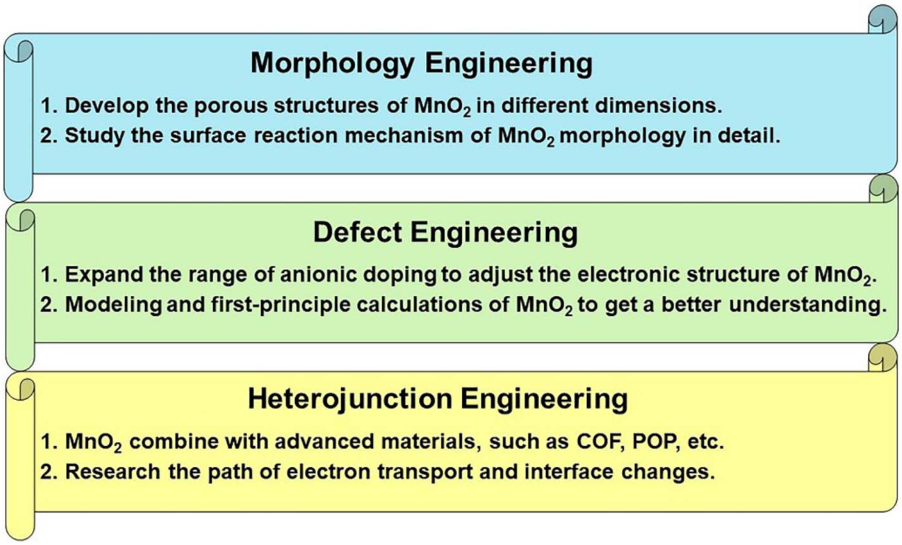
Morphology Engineering
1. Develop the porous structures of MnO_2 in different dimensions.
2. Study the surface reaction mechanism of MnO_2 morphology in detail.

Defect Engineering
1. Expand the range of anionic doping to adjust the electronic structure of MnO_2.
2. Modeling and first-principle calculations of MnO_2 to get a better understanding.

Heterojunction Engineering
1. MnO_2 combine with advanced materials, such as COF, POP, etc.
2. Research the path of electron transport and interface changes.

Fig. 17 Prospects for MnO_2-based electrode materials for SCs.

the porous structure and improving the stability of the structure.[127–132] Up to now, great progress has been made and the exploration of heterojunctions is not over yet, so further efforts are still needed. In the future research process, it can focus on combining MnO_2 with advanced materials (such as COF, POP, *etc.*) to form heterojunction materials. Based on the above basis, advanced characterization methods are used to deeply explore the changes of its electron transport paths and interfaces.

In summary, the reaction mechanisms of MnO_2 as electrode materials for SCs need to be further explored and refined. We sincerely hope that the review will provide an overview of the study progress of MnO_2-based electrode materials for SC and theoretical guidance for subsequent basic and applied research.

Author contributions

Juyin Liu: project conceptualization, methodology, investigation, writing – original draft, writing – review & editing, visualization. Jiali Bao: writing – review & editing. Xin Zhang: writing – review & editing. Yanfang Gao: resources, funding acquisition. Yao Zhang: supervision. Ling Liu: writing – review & editing, resources, funding acquisition. Zhenzhu Cao: writing – review & editing.

Conflicts of interest

There are no conflicts to declare.

Acknowledgements

This work was supported by the National Natural Science Foundation of China (No. 21566030) and Ministry of Science and Technology China-South Africa Joint Research Program (No. CS08-L15), Project of Inner Mongolia Education Department (NJZY089), Natural Science Foundation of Inner Mongolia (2015MS0205), Scientific Research Startup Foundation Project (No. DC2200000899), the National Natural Science Foundation of China (No. 22165021), Scientific Foundation of High Education Institutes Inner Mongolia of China (NJZY20071), and creative talents team of "Prairie Talent" engineering industry and the "Prairie Talent" of organization Department of Inner Mongolia Party Committee.

References

1 P. Simon and Y. Gogotsi, *Nat. Mater.*, 2008, **7**, 845–854.
2 G. Ma, M. Dong, K. Sun, E. Feng, H. Peng and Z. Lei, *J. Mater. Chem. A*, 2015, **3**, 4035–4041.
3 R. M. John and P. Simon, *Science*, 2008, **321**, 651–652.
4 R. Wang, M. Yao and Z. Niu, Smart supercapacitors from materials to devices, *InfoMat*, 2020, **2**, 113–125.
5 Y. Su, N. Li, L. Wang, R. Lin, Y. Zheng, G. Rong and M. Sawan, *Adv. Mater. Technol.*, 2022, **7**, 2100608.
6 M. Shi, C. Yang, X. Song, L. Zhao, J. Liu, P. Zhang and L. Gao, *Adv. Sustainable Syst.*, 2017, **1**, 1700044.
7 R. K. Sarojini, K. Palanisamy, P. Sanjeevikumar and J. B.-H. Nielsen, *IET Renew. Power Gener.*, 2020, **14**, 1156–1163.
8 L. Chai, P. Wang, X. Liu, Y. Sun, X. Li and J. Pan, *J. Power Sources*, 2022, **532**, 231324.
9 X. Gang, M. Krishnamoorthy, W. Jiang, J. Pan, Z. Pan and X. Liu, *Carbon*, 2021, **171**, 62–71.
10 L. Sheng, L. Jiang, T. Wei, Z. Liu and Z. Fan, *Adv. Energy Mater.*, 2017, **7**, 1700668.
11 H. Jin, X. Feng, J. Li, M. Li, Y. Xia, Y. Yuan, C. Yang, B. Dai, Z. Lin, J. Wang, J. Lu and S. Wang, *Angew. Chem., Int. Ed.*, 2019, **58**, 2397–2401.

12 H. S. Kim, J. B. Cook, H. Lin, J. S. Ko, S. H. Tolbert, V. Ozolins and B. Dunn, *Nat. Mater.*, 2017, **16**, 454–460.

13 S. Liu, A. Li, C. Yang, F. Ouyang, J. Zhou and X. Liu, *Appl. Surf. Sci.*, 2022, **571**, 151306.

14 A. Muzaffar, M. B. Ahamed, K. Deshmukh and J. Thirumalai, *Renewable Sustainable Energy Rev.*, 2019, **101**, 123–145.

15 Z. K. He, Y. Lu, C. Zhao, J. Zhao, Z. Gao and Y. Y. Song, *Appl. Surf. Sci.*, 2021, **567**, 150832.

16 M. Y. Chung and C. T. Lo, *Electrochim. Acta*, 2020, **364**, 137324.

17 I. Ryu, D. Kim, G. Choe, S. Jin, D. Hong and S. Yim, *J. Mater. Chem. A*, 2021, **9**, 26172–26180.

18 K. C. Devarayapalli, K. Lee, H. B. Do, N. N. Dang, K. Yoo, J. Shim and S. V. P. Vattikuti, *Mater. Today Energy*, 2021, **21**, 100699.

19 Z. Shi, L. Xing, Y. Liu, Y. Gao and J. Liu, *Carbon*, 2018, **129**, 819–825.

20 M. B. Poudel and H. J. Kim, *J. Energy Chem.*, 2022, **64**, 475–484.

21 Z. Shi, J. Liu, Y. Gao and Y. Xu, *J. Mater. Sci.*, 2021, **56**, 1612–1629.

22 G. Manibalan, Y. Govindaraj, J. Yesuraj, P. Kuppusami, G. Murugadoss, R. Murugavel and M. R. Kumar, *J. Colloid Interface Sci.*, 2021, **585**, 505–518.

23 Y. Zhang, X. Yuan, W. Lu, Y. Yan, J. Zhu and T. W. Chou, *Chem. Eng. J.*, 2019, **368**, 525–532.

24 J. R. Choi, J. W. Lee, G. Yang, Y. J. Heo and S. J. Park, *Catalysts*, 2020, **10**, 256.

25 Y. Mao, J. Xie, C. Guo, H. Liu, H. Xiao and W. Hu, *Chem. Eng. J.*, 2021, **426**, 131188.

26 Y. Wei, M. Zheng, W. Luo, B. Dai, J. Ren, M. Ma, T. Li and Y. Ma, All pseudocapacitive MXene-MnO_2 flexible asymmetric supercapacitor, *J. Energy Storage*, 2022, **45**, 103715.

27 S. G. Mohamed, S. Y. Attia and H. H. Hassan, *Microporous Mesoporous Mater.*, 2017, **251**, 26–33.

28 N. R. Chodankar, D. P. Dubal, Y. Kwon and D.-H. Kim, *NPG Asia Mater.*, 2017, **9**, e419.

29 L. Lin, S. Tang, S. Zhao, X. Peng and N. Hu, *Electrochim. Acta*, 2017, **228**, 175–182.

30 H. Wu, Z. Lou, H. Yang and G. Shen, *Nanoscale*, 2015, **7**, 1921–1926.

31 M. Isacfranklin, S. Daphine, R. Yuvakkumar, L. Kungumadevi, G. Ravi, A. G. Al-Sehemi and D. Velauthapillai, *Ceram. Int.*, 2022, **48**, 24745–24750.

32 Q. Ma, F. Cui, J. Zhang and T. Cui, *J. Colloid Interface Sci.*, 2023, **629**, 649–659.

33 A. K. Das, N. H. Kim, S. H. Lee, Y. Sohn and J. H. Lee, *Composites, Part B*, 2018, **150**, 269–276.

34 A. K. Das, N. H. Kim, S. H. Lee, Y. Sohn and J. H. Lee, *Composites, Part B*, 2018, **150**, 234–241.

35 P. Zhang and H. He, *J. Alloys Compd.*, 2020, **826**, 153993.

36 Y. Dong, Y. Wang, Y. Xu, C. Chen, Y. Wang, L. Jiao and H. Yuan, *Electrochim. Acta*, 2017, **225**, 39–46.

37 X. Zheng, Y. Ye, Q. Yang, B. Geng and X. Zhang, *Dalton Trans.*, 2016, **45**, 572–578.

38 S. Nagamuthu, S. Vijayakumar, S.-H. Lee and K.-S. Ryu, *Appl. Surf. Sci.*, 2016, **390**, 202–208.

39 Q. Zhao, A. Song, S. Ding, R. Qin, Y. Cui, S. Li and F. Pan, Preintercalation Strategy in Manganese Oxides for Electrochemical Energy Storage: Review and Prospects, *Adv. Mater.*, 2020, **32**, 2002450.

40 J. Shin, J. K. Seo, R. Yaylian, A. Huang and Y. S. Meng, *Int. Mater. Rev.*, 2019, 1–32.

41 V. Veeramani, B. Dinesh, S. M. Chen and R. Saraswathi, *J. Mater. Chem. A*, 2016, **4**, 3304–3315.

42 S. B. Singh, T. I. Singh, N. H. Kim and J. H. Lee, *J. Mater. Chem. A*, 2019, **7**, 10672–10683.

43 S. Sun, G. Jiang, Y. Liu, B. Yu and U. Evariste, *J. Energy Storage*, 2018, **18**, 256–258.

44 A. Kumar, A. Thomas, A. Gupta, M. Garg, J. Singh, G. Perumal, E. Sujithkrishnan, P. Elumalai and H. S. Arora, *J. Energy Storage*, 2021, **42**, 103100.

45 K. Xiao, J. W. Li, G. F. Chen, Z. Q. Liu, N. Li and Y.-Z. Su, *Electrochim. Acta*, 2014, **149**, 341–348.

46 Y. Wang, Y. Wang and L. Jiang, *J. Appl. Electrochem.*, 2018, **48**, 495–507.

47 M. J. Deng, P. J. Ho, C. Z. Song, S. A. Chen, J. F. Lee, J. M. Chen and K. T. Lu, *Energy Environ. Sci.*, 2013, **6**, 2178–2185.

48 J. Cao, Y. Wang, Y. Zhou, J. H. Ouyang, D. Jia and L. Guo, *J. Electroanal. Chem.*, 2013, **689**, 201–206.

49 S. Sun, P. Wang, S. Wang, Q. Wu and S. Fang, *Mater. Lett.*, 2015, **145**, 141–144.

50 Z. Liu, J. Zhang, X. Yang, Y. He, Y. Bai, L. Kang, H. Xu, F. Shi and Z. Lei, *J. Mater. Chem. A*, 2016, **4**, 9088–9096.

51 C. Choi, H. J. Sim, G. M. Spinks, X. Lepró, R. H. Baughman and S. J. Kim, *Adv. Energy Mater.*, 2016, **6**, 1502119.

52 T. Park, Y. Jang, J. W. Park, H. Kim and S. J. Kim, *RSC Adv.*, 2020, **10**, 14007–14012.

53 M. Liu, L. Gan, W. Xiong, Z. Xu, D. Zhu and L. Chen, *J. Mater. Chem. A*, 2014, **2**, 2555–2562.

54 M. Li, J. Yu, X. Wang and Z. Yang, *Appl. Surf. Sci.*, 2020, **530**, 147230.

55 S. Devaraj and N. Munichandraiah, *J. Phys. Chem. C*, 2008, **112**, 4406–4417.

56 S. D. Huang, C. Shang, X. J. Zhang and Z. P. Liu, *Chem. Sci.*, 2017, **8**, 6327–6337.

57 W. Yao, G. M. Odegard, Z. Huang, Y. Yuan, H. Asayesh-Ardakani, S. Sharifi-Asl, M. Cheng, B. Song, R. Deivanayagam, F. Long, C. R. Friedrich, K. Amine, J. Lu and R. Shahbazian-Yassar, *Nano Energy*, 2018, **48**, 301–311.

58 T. Barudžija, V. Kusigerski, N. Cvjetićanin, S. Šorgić, M. Perović and M. Mitrić, *J. Alloys Compd.*, 2016, **665**, 261–270.

59 R. Yang, Y. Fan, R. Ye, Y. Tang, X. Cao, Z. Yin and Z. Zeng, *Adv. Mater.*, 2021, **33**, 2004862.

60 M. T. N. Dinh, C. C. Nguyen, T. L. T. Vu, V. T. Ho and Q. D. Truong, *Appl. Catal., A*, 2020, **595**, 117473.

61 X. Wang and Y. Li, *Chem. Commun.*, 2002, 764–765.

62 Y. Chabre and J. Pannetier, *Prog. Solid State Chem.*, 1995, **23**, 1–130.

63 J. Zhao, Z. Tao, J. Liang and J. Chen, *Cryst. Growth Des.*, 2008, **8**, 2799–2805.

64 S. L. Brock, N. Duan, Z. R. Tian, O. Giraldo, H. Zhou and S. L. Suib, *Chem. Mater.*, 1998, **10**, 2619–2628.

65 C. H. Kim, Z. Akase, L. Zhang, A. H. Heuer, A. E. Newman and P. J. Hughes, *J. Solid State Chem.*, 2006, **179**, 753–774.

66 J. Greedan, N. Raju, A. Wills, C. Morin, S. Shaw and J. Reimers, *Chem. Mater.*, 1998, **10**, 3058–3067.

67 J. Wan, P. Ji, B. Li, Y. Xi, X. Gu, L. Huang, M. He and C. Hu, *Chem. Commun.*, 2022, **58**, 589–592.

68 Q. Qu, P. Zhang, B. Wang, Y. Chen, S. Tian, Y. Wu and R. Holze, *J. Phys. Chem. C*, 2009, **113**, 14020–14027.

69 H. Jiang, P. S. Lee and C. Li, *Energy Environ. Sci.*, 2013, **6**, 41–53.

70 T. Brousse, D. Bélanger and J. W. Long, *J. Electrochem. Soc.*, 2015, **162**, A5185–A5189.

71 X. Liu, Y. Zheng and X. Wang, *Chem.–Eur. J.*, 2015, **21**, 10408–10415.

72 W. Huo, X. Liu and Y. Zhang, *Nanoscale Adv.*, 2019, **2**, 37–54.

73 Z. Sun, Y. Zhang, Y. Liu, J. Fu, S. Cheng, P. Cui and E. Xie, *J. Power Sources*, 2019, **436**, 226795.

74 M. Huang, F. Li, F. Dong, Y. X. Zhang and L. L. Zhang, *J. Mater. Chem. A*, 2015, **3**, 21380–21423.

75 T. Brousse, M. Toupin, R. Dugas, L. Athouël, O. Crosnier and D. Bélanger, *J. Electrochem. Soc.*, 2006, **153**, A2171.

76 K. Chen, C. Sun and D. Xue, *Phys. Chem. Chem. Phys.*, 2014, **17**, 732–750.

77 K. Naoi and P. Simon, *Electrochem. Soc. Interface*, 2008, **17**, 34.

78 J. Shin, J. K. Seo, R. Yaylian, A. Huang and Y. S. Meng, *Int. Mater. Rev.*, 2020, **65**, 356–387.

79 B. S. Singu and K. R. Yoon, *J. Alloys Compd.*, 2017, **695**, 771–778.

80 N. Tang, X. Tian, C. Yang and Z. Pi, *Mater. Res. Bull.*, 2009, **44**, 2062–2067.

81 B. Yin, S. Zhang, Y. Jiao, Y. Liu, F. Qu and X. Wu, *CrystEngComm*, 2014, **16**, 9999–10005.

82 M. Xu, L. Kong, W. Zhou and H. Li, *J. Phys. Chem. C*, 2007, **111**, 19141–19147.

83 W. Xie, J. Wang, X. Long, X. Wang, S. Zou, L. Zhang, H. Xu, Y. Fu, D. Liu, Y. Li, J. Li and D. He, *J. Energy Storage*, 2021, **35**, 102308.

84 L. Athouël, F. Moser, R. Dugas, O. Crosnier, D. Bélanger and T. Brousse, *J. Phys. Chem. C*, 2008, **112**, 7270–7277.

85 J. Zhu, W. Shi, N. Xiao, X. Rui, H. Tan, X. Lu, H. H. Hng, J. Ma and Q. Yan, *ACS Appl. Mater. Interfaces*, 2012, **4**, 2769–2774.

86 R. E. John, A. Chandran, M. Thomas, J. Jose and K. C. George, *Appl. Surf. Sci.*, 2016, **367**, 43–51.

87 M. Khosravi, H. Feizi, R. Bagheri, Z. Song, B. Haghighi and M. M. Najafpour, *New J. Chem.*, 2019, **43**, 4049–4058.

88 T. Xiong, Y. Zhang, W. S. V. Lee and J. Xue, *Adv. Energy Mater.*, 2020, **10**, 2001769.

89 Y. P. Zhu, C. Xia, Y. Lei, N. Singh, U. Schwingenschlögl and H. N. Alshareef, *Nano Energy*, 2019, **56**, 357–364.

90 A. Zhang, R. Gao, L. Hu, X. Zang, R. Yang, S. Wang, S. Yao, Z. Yang, H. Hao and Y. M. Yan, *Chem. Eng. J.*, 2021, **417**, 129186.

91 R. Samal, M. Kandasamy, B. Chakraborty and C. S. Rout, *Int. J. Hydrogen Energy*, 2021, **46**, 28028–28042.

92 F. Jing, Z. Ma, J. Wang, Y. Fan, X. Qin and G. Shao, *Chem. Eng. J.*, 2022, **435**, 135103.

93 D. Rolison and L. Nazar, *MRS Bull.*, 2011, **36**, 486–493.

94 H. Wang, J. Zhang, X. Hang, X. Zhang, J. Xie, B. Pan and Y. Xie, *Angew. Chem., Int. Ed.*, 2014, **127**, 1195–1199.

95 P. Gao, P. Metz, T. Hey, Y. Gong, D. Liu, D. D. Edwards, J. Y. Howe, R. Huang and S. T. Misture, *Nat. Commun.*, 2017, **8**, 14559.

96 L. T. Tseng, Y. Lu, H. M. Fan, Y. Wang, X. Luo, T. Liu, P. Munroe, S. Li and J. Yi, *Sci. Rep.*, 2015, **5**, 9094.

97 S. Yao, R. Zhao, S. Wang, Y. Zhou, R. Liu, L. Hu, A. Zhang, R. Yang, X. Liu, Z. Fu, D. Wang, Z. Yang and Y.-M. Yan, *Chem. Eng. J.*, 2022, **429**, 132521.

98 X. Zhang, X. Liu, Y. Zeng, Y. Tong and X. Lu, *Small Methods*, 2020, **4**, 1900823.

99 H. Z. Chi, Y. Li, Y. Xin and H. Qin, *Chem. Commun.*, 2014, **50**, 13349–13352.

100 S. Chen, Y. Xiang, W. Xu and C. Peng, *Inorg. Chem. Front.*, 2019, **6**, 199–208.

101 W. Zhang, Y. Yang, R. Xia, Y. Li, J. Zhao, L. Lin, J. Cao, Q. Wang, Y. Liu and H. Guo, *Carbon*, 2020, **162**, 114–123.

102 N. Zhang, C. Xu, H. Wang, J. Zhang, Y. Liu and Y. Fang, *J. Mater. Sci.: Mater. Electron.*, 2021, **32**, 1787–1799.

103 G. Luo, *Int. J. Electrochem. Sci.*, 2020, **15**, 515–525.

104 L. Khandare and S. Terdale, *Appl. Surf. Sci.*, 2017, **418**, 22–29.

105 W. Lu, Y. Li, M. Yang, X. Jiang, Y. Zhang and Y. Xing, *ACS Appl. Energy Mater.*, 2020, **3**, 8190–8197.

106 L. Kang, C. Huang, J. Zhang, M. Zhang, N. Zhang, Y. He, C. Luo, C. Wang, X. Zhou and X. Wu, *Composites, Part B*, 2019, **178**, 107501.

107 M. Huang, Y. Zhang, F. Li, Z. Wang, Alamusi, N. Hu, Z. Wen and Q. Liu, *Sci. Rep.*, 2014, **4**, 4518.

108 M. Huang, F. Li, X. L. Zhao, D. Luo, X. Q. You, Y. X. Zhang and G. Li, *Electrochim. Acta*, 2015, **152**, 172–177.

109 R. Rajagopal and K.-S. Ryu, *J. Electroanal. Chem.*, 2020, **856**, 113669.

110 X. Y. Cao, X. Xing, N. Zhang, H. Gao, M. Y. Zhang, Y. C. Shang and X. T. Zhang, *J. Mater. Chem. A*, 2015, **3**, 3785–3793.

111 X. Zheng, Z. Han, W. Yang, F. Qu, B. Liu and X. Wu, *Dalton Trans.*, 2016, **45**, 16850–16858.

112 H. Du, C. Wang and J. Lv, *Solid State Commun.*, 2018, **277**, 19–24.

113 P. M. Shafi, R. Dhanabal, A. Chithambararaj, S. Velmathi and A. C. Bose, *ACS Sustainable Chem. Eng.*, 2017, **5**, 4757–4770.

114 J. Zhu, D. Zhang, Z. Zhu, Q. Wu and J. Li, *Ionics*, 2021, **27**, 3699–3714.

115 Z. J. Fan, J. Yan, F. Wei, G. Q. Ning, L. J. Zhi, J. C. Liu, D. X. Cao and G. L. Wang, *ACS Nano*, 2011, **5**, 2787–2794.

116 S. Jangu, B. K. Satpathy, M. Raju, C. Jacob and D. Pradhan, *Dalton Trans.*, 2021, **50**, 6878–6888.

117 H. W. Chang, Y. C. Huang, J. L. Chen, C. L. Chen, J. M. Chen, D. H. Wei, W. C. Chou, C. L. Dong and Y. C. Tsai, *Catal. Today*, 2022, **388**, 63–69.

118 X. L. Bai, Y. L. Gao, Z. Y. Gao, J. Y. Ma, X. L. Tong, H. B. Sun and J. A. Wang, *Appl. Phys. Lett.*, 2020, **117**, 183901.

119 J. Xu, K. Hou, Z. Ju, C. Ma, W. Wang, C. Wang, J. Cao and Z. Chen, *J. Electrochem. Soc.*, 2017, **164**, A430–A437.

120 H. Lv, X. Gao, Q. Xu, H. Liu, Y. G. Wang and Y. Xia, *ACS Appl. Mater. Interfaces*, 2017, **9**, 40394–40403.

121 A. Prasath, M. Athika, E. Duraisamy, A. S. Sharma and P. Elumalai, *ChemistrySelect*, 2018, **3**, 8713–8723.

122 W. S. Li, M. L. Chang, K. C. Chuang, Y. S. Li, J. D. Luo and H. C. Cheng, *J. Electrochem. Soc.*, 2019, **166**, A2194–A2198.

123 D. Gueon and J. H. Moon, *ACS Sustainable Chem. Eng.*, 2017, **5**, 2445–2453.

124 K. Zhao, Z. Xu, Z. He, G. Ye, Q. Gan, Z. Zhou and S. Liu, *J. Mater. Sci.*, 2018, **53**, 13111–13125.

125 Y. Chen, C. Kang, L. Ma, L. Fu, G. Li, Q. Hu and Q. Liu, *Chem. Eng. J.*, 2021, **417**, 129243.

126 J. Fu, Y. Zhang, H. Zhao, R. Jiang and R. Zhang, *J. Colloid Interface Sci.*, 2020, **559**, 39–44.

127 N. Liu, Y. Su, Z. Wang, Z. Wang, J. Xia, Y. Chen, Z. Zhao, Q. Li and F. Geng, *ACS Nano*, 2017, **11**, 7879–7888.

128 J. Li, C. Wei, Y. Sun, Q. Liu, X. Zhang and J. Guo, *Adv. Mater. Interfaces*, 2019, **6**, 1801470.

129 H. Wang, G. Yan, X. Cao, Y. Liu, Y. Zhong, L. Cui and J. Liu, *J. Colloid Interface Sci.*, 2020, **563**, 394–404.

130 M. Cui, S. Tang, Y. Ma, X. Shi, J. A. Syed and X. Meng, *J. Power Sources*, 2018, **396**, 483–490.

131 K. Adaikalam, S. Ramesh, P. Santhoshkumar, H. S. Kim, H.-C. Park and H.-S. Kim, *Int. J. Energy Res.*, 2022, **46**, 4494–4505.

132 H. Gao, S. Cao and Y. Cao, *Electrochim. Acta*, 2017, **240**, 31–42.

133 X. Jia, X. Wu and B. Liu, *Dalton Trans.*, 2018, **47**, 15506–15511.

134 M. Jiang, C. Fu, J. Yang, Q. Liu, J. Zhang and B. Sun, *Energy Storage Mater.*, 2019, **18**, 34–42.